ORIGINAL PAPER

Seismic Stability Assessment of Rock Slopes Using Limiting Slope Face Concept

Shibsankar Nandi[1] · Priyanka Ghosh[1]

Abstract

This study communicates a novel seismic stability assessment of rock slopes based on the concept of the limiting slope face (LSF) combined with the method of stress characteristics (MSC) and the modified pseudo-dynamic (MPD) approach. The slope geometry with a target factor of safety (FS) of 1.0 is derived, precluding the need for any preordained slip surfaces in the analysis. Subsequently, the derived LSF in cognition with the morphological aspects indeed acts as a self-guided stability index for rock slopes. Besides, a realistic characterization of the dynamic properties of input earthquake motions satisfying the zero stress boundary conditions is apprehended through the coherent utilization of the MPD approach. The generalized Hoek–Brown (GHB) strength criterion is engaged to capture the factual non-linearity present in the rock strength. Compared to the reported investigations, the present results indicate that the developed curvilinear LSFs are steeper than the traditional linear slopes commonly encountered in the conventional practice. A parametric study accounting for the effect of different influential parameters on the behavior of LSFs is performed in view of various prospective design challenges in rock engineering. With a rise in the horizontal seismic acceleration coefficient (k_h) from 0.1 to 0.3, a nearly threefold increase in the magnitude of the major principal stress orientation (ψ) at the slope crest but along the slope can be observed. Such enhancement in ψ indicates significantly flat LSF. A sudden rise in the magnitude of ψ can also be observed at the fundamental frequencies of seismic waves due to resonance. However, at $k_h = 0.1$, such aptness declines by 54% at the first fundamental frequency of the shear wave as the rock mass damping increases from 5 to 15%. Thus, the present approach attributes to a rational way for seismic design and stability assessment of rock slopes. Several real-life case studies adopting the current LSF concept further exhibit the accuracy, rationality, and robustness of the proposed methodology.

Highlights

- Concept of limiting slope face is introduced for the seismic performance of rock slopes.
- Analysis is performed using an integrated framework of generalized Hoek-Brown criterion, method of stress characteristics and modified pseudo-dynamic approach.
- An adaptive collapse mechanism is investigated in response to varying seismic wave characteristics and rock mass parameters.
- A comprehensive review of other prevailing analytical seismic approaches is provided.
- Rationality of the results is ensured through validation with different published case studies.

✉ Priyanka Ghosh
priyog@iitk.ac.in

1   Department of Civil Engineering, Indian Institute of Technology, Kanpur 208 016, India

List of Symbols

α	Horizontal inclination of a linear slope
α_h	Non-dimensional horizontal seismic acceleration normalized with respect to g
α_v	Non-dimensional vertical seismic acceleration normalized with respect to g

β_a A parameter as defined in Eq. (9)

γ Unit weight of the rock mass

δ A parameter as defined in Eq. (23)

ζ_a A parameter as defined in Eq. (9)

θ Angle made by the major principal stress with the positive z-axis

θ_g Magnitude of θ along the top surface of the slope (OG)

θ_s Magnitude of θ along the limiting slope face (OA)

μ A parameter as defined in Eq. (15)

ξ Damping ratio of the rock mass

ρ Instantaneous friction angle as defined in Eq. (17)

ρ_g Magnitude of ρ along the top surface of the slope (OG)

ρ_s Magnitude of ρ along the limiting slope face (OA)

σ^+, σ^- Axes in the two-dimensional curvilinear coordinate system representing the positive and negative characteristics, respectively

σ_1 Major principal stress

σ_3 Minor principal stress

σ_{ci} Uniaxial compressive strength of the intact rock

σ_{ng} Normal stress on the top surface of the slope (OG)

σ_x Normal stress on the x plane

σ_z Normal stress on the z plane

τ_g Shear stress on the top surface of the slope (OG)

τ_{xz} Shear stress in the xz plane

χ Horizontal inclination of the top surface of the slope (OG), as shown in Fig. 15a

ψ Magnitude of θ along the limiting slope face (OA), but at the slope crest (O)

ω Angular frequency of seismic waves $= 2\pi/T$

a Dimensionless Hoek–Brown material parameter, as defined in Eq. (7a), representing the characteristics of rock mass

$a_h(z, t)$ Horizontal seismic acceleration in the rock mass at depth z and time t

$a_v(z, t)$ Vertical seismic acceleration in the rock mass at depth z and time t

A_a A parameter as defined in Eq. (9)

C_p, C_{pz} Dimensionless parameters, as defined in Eqs. (4b) and (4a), respectively

C_s, C_{sz} Dimensionless parameters, as defined in Eqs. (3b) and (3a), respectively

d Depth of rigid bed from the base of the slope

D Disturbance factor of the rock mass

f Macroscopic yield condition

f_a Amplification factor for seismic waves

F Function defining the yield criterion in Eq. (12)

g Acceleration due to gravity

GSI Geological strength index

h Height of the slope having a horizontal top surface (OG), as shown in Fig. 1a

h' Height of the slope having an inclined top surface (OG), as shown in Fig. 15a

H Depth of the rigid bed from the top surface (OG) of the slope

k A parameter as defined in Eq. (9)

k_h Horizontal seismic acceleration coefficient

k_v Vertical seismic acceleration coefficient

m A parameter as defined in Eq. (15)

m_b Dimensionless Hoek–Brown material parameter, as defined in Eq. (7b)

m_i Hoek–Brown constant of intact rock representing the hardness of the rock

N Stability number $= \sigma_{ci}/(\gamma h.\text{FS})$

N_{cr} Critical stability number corresponding to FS $= 1.0$

p Average stress

p_g Magnitude of p along the top surface of the slope (OG)

p_s Magnitude of p along the limiting slope face (OA)

q Uniformly distributed surcharge

R Radius of the Mohr circle

R_g Magnitude of R along the top surface of the slope (OG)

R_s Magnitude of R along the limiting slope face (OA)

s Dimensionless Hoek–Brown material parameter as defined in Eq. (7c) representing the degree of fragmentation of rock

S_p, S_{pz} Dimensionless parameters, as defined in Eqs. (4b) and (4a), respectively

S_s, S_{sz} Dimensionless parameters, as defined in Eqs. (3b) and (3a), respectively

t Time

T Period of lateral shaking

$u_h(z, t)$ Horizontal displacement of the rock mass at depth z and time t

$u_v(z, t)$ Vertical displacement of the rock mass at depth z and time t

u_{h0}, u_{v0} Amplitudes of the finite harmonic displacement at the rigid base along the horizontal and the vertical directions, respectively

u_{hb}, u_{vb} Finite harmonic displacements at the rigid base along the horizontal and the vertical directions, respectively

V_p Velocity of primary wave

V_s Velocity of shear wave

x, z Axes in the regular two-dimensional Cartesian coordinate system

x', z' Axes in the transformed two-dimensional Cartesian coordinate system, as shown in Fig. 15a

y_{s1}, y_{s2} Dimensionless parameters, as defined in Eq. (3c)

y_{p1}, y_{p2} Dimensionless parameters as defined in Eq. (4c)

X Body force per unit volume in the x-direction

Z Body force per unit volume in the z-direction

1 Introduction

Evaluation of the rock slope stability in seismically active regions is a crucial design consideration for various engineering structures, such as bridges, dams, open pits/mines, roads, and tunnels, to ensure the safe and satisfactory performance of the systems. The Mononobe–Okabe method (Okabe 1926; Mononobe and Matsuo 1929) or the pseudo-static (PS) approach is usually recommended for reckoning the earthquake effect on the rock slope stability due to its remarkable simplicity. To ensure a simplistic analysis, the PS approach primarily surmises the seismic inertia forces to be constant and uniform across the entire rock mass (Yang et al. 2004; Li et al. 2009; Latha and Garaga 2010; Jiang et al. 2016; Tiwari and Latha 2016; Belghali et al. 2017; Sun et al. 2020; Sarkar and Chakraborty 2021; Singh et al. 2022; Wallace et al. 2022; Wang et al. 2022b). However, naturally, a random vibration, such as an earthquake, is barely stationary. The induced earthquake acceleration, an obvious function of time and space, contradicts the oversimplification thus cast in the PS approach (Qin and Chian 2018; Fan et al. 2019; Gu and Wu 2019). On the contrary, quite a few studies (Latha and Garaga 2010; Sun et al. 2012; Gischig et al. 2015; Zhang et al. 2015; Zhao et al. 2017; Luo et al. 2020) addressed a more reliable seismic response of rock slopes utilizing the on-site earthquake ground motion records associated with an appropriate constitutive model. However, the enormous computational rigor accompanying such dynamic time-history analyses conversely condenses its flexibility for a routine engineering application. Hence, to capture the essence of seismic accelerations with a reasonable effort, the pseudo-dynamic approach is often preferred as a worthy trade-off between the simplistic PS method and the rigorous dynamic time-history analysis.

Steedman and Zeng (1990), and Choudhury and Nimbalkar (2005) proposed the original pseudo-dynamic (OPD) approach, where a sinusoidal wave was commonly considered to accommodate the phase change in shear waves propagating through a vibrating medium. Later, Zeng and Steedman (1993) substantiated the legitimacy of the OPD approach, comparing the theoretical outcomes with a group of centrifuge model test results. Subsequently, several researchers (Choudhury and Nimbalkar 2005; Nimbalkar et al. 2006; Xu et al. 2017) contributed to the OPD

approach by considering the effect of both shear and primary waves. Qin and Chian (2018) applied the OPD approach to determine the seismic bearing capacity of Hoek–Brown rock slopes. Additionally, Sun et al. (2022) and Wang et al. (2022a) evaluated the pseudo-dynamic safety factor of slopes in the Hoek–Brown medium utilizing the OPD approach. However, the OPD approach suffers from two intrinsic limitations: violation of the zero stress boundary conditions at the ground surface and approximate linear amplification profile for propagating seismic waves. To overcome such shortcomings of the OPD approach, Bellezza (2014, 2015) introduced the modified pseudo-dynamic (MPD) approach based on a more realistic idealization of the energy dissipation characteristics of the medium modeled as the Kelvin–Voigt material. Later, the efficacy of the MPD approach was established by several researchers (Pain et al. 2017; Rajesh and Choudhury 2017; Srikar and Mittal 2020) in solving different geotechnical problems. However, limited studies were conducted deploying the MPD approach in a specific context of rock slopes. Gu and Wu (2019) implemented the MPD approach alongside the non-linear twin shear criterion to analyze the seismic stability of waterfront rock slopes. Zhao et al. (2020) performed a reliability-based slope stability analysis under the combined framework of the Barton–Bandis failure criterion and the MPD approach. Zhong and Yang (2021) presented the seismic stability of rock slopes considering the Hoek–Brown strength criterion and the MPD approach.

Most of the studies discussed above extensively utilized the limit equilibrium (LE) or the limit analysis (LA) method while analyzing the seismic stability of rock slopes. Hence, inevitable inadequacy, such as predestined slip surfaces assumed prior to the analysis (Yang et al. 2004; Jiang et al. 2016; Belghali et al. 2017; Gu and Wu 2019), inevitably exists in the previous formulations, apart from the inherent shortcomings of the PS and the OPD approaches. In addition, an approximated state of stress, even if not aligned with the conditions of the static equilibrium, can also be observed alongside such presumed slip surfaces (Zhong and Yang 2021). Besides, the LE method overestimates the stability of rock slopes, especially in the case of steeper rock slopes and poor-quality rock masses (Li et al. 2009, 2022). By employing the finite-element limit analysis (FELA), several previous investigations (Li et al. 2009, 2022; Kumar and Rahaman 2020; Wu et al. 2021) endeavored to avoid the above-mentioned discrepancies. However, the accuracy is utterly earned at the cost of an enhanced numerical computation over an excessive requirement of input parameters, even for a simple preliminary analysis of homogeneous slopes (Yang and Zou 2006). In contrast, the method of stress characteristics (MSC), a plasticity-based classical approach, emerges as a compelling choice to tackle the above-mentioned limitations. Sokolovski (1960) introduced
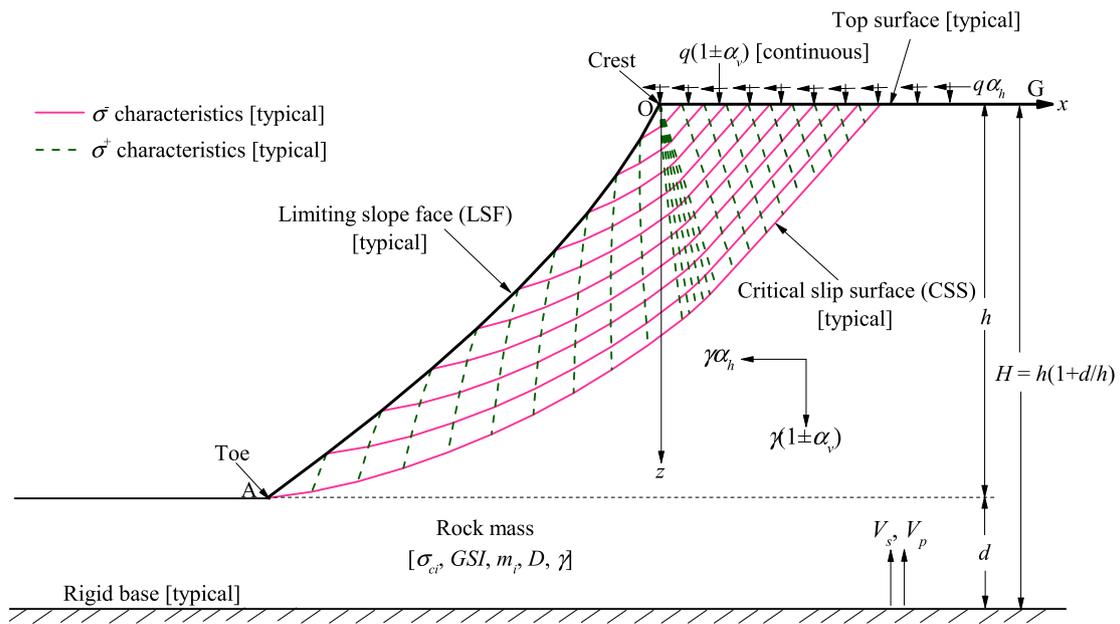
(a)
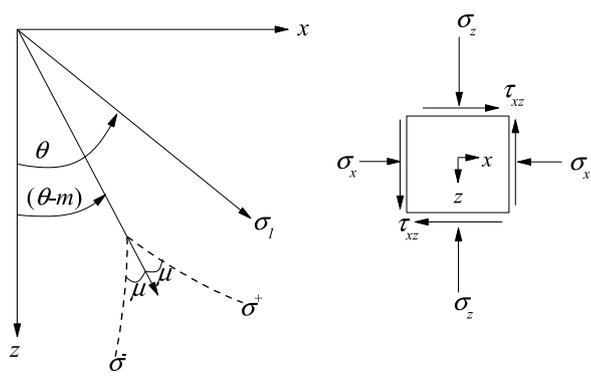
(b)
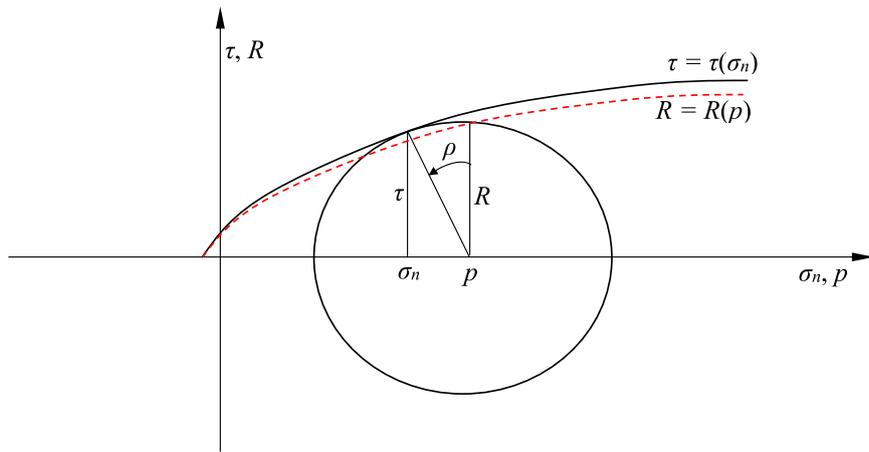
(c)

Fig. 1 **a** Problem idealization with associated collapse mechanism; **b** state of stress and sign convention; **c** Mohr-circle envelope at failure for non-linear generalized Hoek–Brown criterion

the MSC for the soil media. Later, Serrano and Olalla (1994) extended the method in the domain of classical rock mechanics to investigate the bearing capacity of strip footings resting on a weightless rock medium. Subsequently, several studies (Serrano et al. 2000; Kumar and Mohan Rao 2003; Jahanandish and Keshavarz 2005; Veiskarami et al. 2014; Keshavarz et al. 2016; Keshavarz and Kumar 2018, 2021; Li et al. 2019; Santhoshkumar et al. 2019; Santhoshkumar and Ghosh 2020; Nandi et al. 2021a, b) accounting for various stability-related geotechnical problems were performed using the MSC. In addition, based on the MSC, Sokolovski (1960) initiated a novel concept of the limiting slope face (LSF), anticipating a target factor of safety (FS) of 1.0 for the static stability analysis of soil slopes. Later, Nandi et al. (2021a, b) improvised the concept of the LSF for soil slopes by coupling it with the OPD and MPD approaches, respectively. However, the seismic stability analysis of rock slopes utilizing the concept of the LSF remains almost untraversed.

Further, there may be better choices than the commonly adopted Mohr–Coulomb (MC) failure criterion for rocks. Instead, the generalized Hoek–Brown (GHB) strength criterion (Hoek and Brown 1980; Hoek et al. 2002) is preferred to model the strength characteristics of intact rocks and uniformly jointed rock mass systems. Experimental investigations generally endorse an omnipresent existence of the strength non-linearity for geo-materials, especially in low confining stresses (Fu and Liao 2010; Shen et al. 2012). However, some recent studies (Qin and Chian 2018; Xu et al. 2018; Sarkar and Chakraborty 2021; Sun et al. 2022; Wang et al. 2022a) adopted a linear approximation of the GHB criterion through a generalized tangential technique or equivalent Mohr–Coulomb criterion. Such linear substitution of the GHB criterion through an equivalent set of the MC parameters was reported to cause an overestimation of the rock slope stability (Li et al. 2009; Zhao et al. 2017; Renani and Martin 2020). Limited attempts (Li et al. 2009; Jiang et al. 2016; Zhong and Yang 2021) were made to consider the non-linearity of the GHB criterion. However, the calculation model was restricted to the LE, LA, or FELA method. Consequently, a coupling between the GHB strength criterion and the MSC alongside the MPD approach urges to be established for a better perspective.

The seismic performance of rock slopes with a specific geometry is often appraised by determining various parameters, such as a factor of safety, stability number, critical earthquake acceleration, seismic ultimate bearing capacity, and seismic displacement. Instead of the aforesaid stability measures, this study introduces a novel LSF-based stability concept employing a combined framework of the MSC and the MPD approach. Accordingly, a precise prediction of the limiting collapse based on FS = 1.0 is ensured in this study. By employing the MSC, the assumption of predestined slip surfaces is ruled out in the analysis. In addition, the effect of seismic waves, excitation frequency, and damping characteristics of the rock mass system are suitably incorporated using the MPD approach. A variable rigid bed below the slope base is duly considered to handle horizontal and vertical seismic accelerations. The curvilinear LSF evolved from the present methodology is found to be morphologically congruent (Gray 2013; Wu and Utili 2015). The results are also presented by employing both PS and OPD approaches to manifest the versatility of the MPD method. Different real-life case studies are validated to establish the potential of the current methodology anticipating the state of the limiting stability in advance.

2 Problem Statement and Assumptions

Figure 1a illustrates a finite rock slope of height, h resting on a rigid bed of depth, d from the base of the slope. The slope supports a uniformly distributed surcharge, q, at the horizontal top surface (OG) and is exposed to a harmonic base excitation under seismic conditions. The rock mass is characterized by the intact uniaxial compressive strength σ_{ci}, the geological strength index GSI, the intact rock yield parameter m_i, the disturbance factor D, and the unit weight γ. According to the previous investigations, this study considers reasonable assumptions of the rock mass homogeneity and isotropy (Yang et al. 2004; Li et al. 2009; Sun et al. 2020; Sarkar and Chakraborty 2021). The strength of the rock mass is assumed to be governed by the GHB criterion. The principal objective is to determine the curvilinear geometry of the rock slope (OA), upholding the condition of the limiting collapse under the induced earthquake inertial effect. As mentioned earlier, the LSF thus derived corresponds to FS = 1.0. In association with the MPD approach, the analysis is executed by establishing a network of stress characteristics, which further assists in obtaining a robust collapse mechanism considering the effect of the frequency of seismic waves, the phase difference, and the rock mass damping.

3 Analysis

3.1 Modified Pseudo-dynamic Approach

Following Bellezza (2014, 2015), the solution to wave propagation problems in visco-elastic rock slopes can be devised by modeling the rock mass as the Kelvin–Voigt material (Kramer 1996). Based on this model, a material damping ratio (ξ) is incorporated to manifest the energy dissipation characteristics of the medium under earthquake conditions. Additionally, resulting shear (S) and primary (P) waves are

assumed to propagate through the medium vertically along the z-axis with velocities V_s and V_p, respectively. Subsequently, the governing equation of motion can be solved for a harmonic base shaking with an angular frequency (ω) and a time period ($T = 2\pi/\omega$) by satisfying the boundary conditions. The aforesaid boundary conditions are a) stress-free boundary conditions along the top surface ($z = 0$); and b) finite harmonic displacements (u_{hb}, u_{vb}) at the rigid base ($z = H$), as given in Eq. (1a, 1b)

$$u_{hb} = u_{h0}\cos(\omega t)(\text{for } S - \text{wave}) \tag{1a}$$

$$u_{vb} = u_{v0}\cos(\omega t)(\text{for } P - \text{wave}). \tag{1b}$$

By imposing the boundary conditions, the solution for the SPATIO-temporal variation in horizontal and vertical displacements (u_h, u_v) of the medium at any depth, z, and at any instant, t can be expressed as (Bellezza 2014, 2015; Pain et al. 2017; Rajesh and Choudhury 2017)

$$u_h(z,t) = \frac{u_{h0}}{C_s^2 + S_s^2}\left[(C_s C_{sz} + S_s S_{sz})\cos(\omega t) + (S_s C_{sz} - C_s S_{sz})\sin(\omega t)\right] \text{ (for } S - \text{wave)} \tag{2a}$$

$$u_v(z,t) = \frac{u_{v0}}{C_p^2 + S_p^2}\left[(C_p C_{pz} + S_p S_{pz})\cos(\omega t) + (S_p C_{pz} - C_p S_{pz})\sin(\omega t)\right] \text{ (for } P - \text{wave)}, \tag{2b}$$

where for S-wave [Eq. (2a)]

$$C_{sz} = \cos\left(\frac{y_{s1}z}{H}\right)\cosh\left(\frac{y_{s2}z}{H}\right); \\ S_{sz} = -\sin\left(\frac{y_{s1}z}{H}\right)\sinh\left(\frac{y_{s2}z}{H}\right) \tag{3a}$$

$$C_s = \cos(y_{s1})\cosh(y_{s2}); \quad S_s = -\sin(y_{s1})\sinh(y_{s2}) \tag{3b}$$

$$y_{s1} = \frac{\omega H}{V_s}\sqrt{\left(\frac{\sqrt{(1+4\xi^2)}+1}{2(1+4\xi^2)}\right)}; \\ y_{s2} = -\frac{\omega H}{V_s}\sqrt{\left(\frac{\sqrt{(1+4\xi^2)}-1}{2(1+4\xi^2)}\right)}, \tag{3c}$$

for P-wave [Eq. (2b)]

$$C_{pz} = \cos\left(\frac{y_{p1}z}{H}\right)\cosh\left(\frac{y_{p2}z}{H}\right); \\ S_{pz} = -\sin\left(\frac{y_{p1}z}{H}\right)\sinh\left(\frac{y_{p2}z}{H}\right) \tag{4a}$$

$$C_p = \cos(y_{p1})\cosh(y_{p2}); \quad S_p = -\sin(y_{p1})\sinh(y_{p2}) \tag{4b}$$

$$y_{p1} = \frac{\omega H}{V_p}\sqrt{\left(\frac{\sqrt{(1+4\xi^2)}+1}{2(1+4\xi^2)}\right)}; \\ y_{p2} = -\frac{\omega H}{V_p}\sqrt{\left(\frac{\sqrt{(1+4\xi^2)}-1}{2(1+4\xi^2)}\right)}. \tag{4c}$$

In Eqs. (3c) and (4c), y_{s1}, y_{s2}, y_{p1}, and y_{p2} are the non-dimensional entities represented as a function of the damping ratio (ξ) and the normalized frequencies ($\omega H/V_s$, $\omega H/V_p$) for S- and P-waves, respectively; H is the depth of the rigid bed from the top surface of the slope (OG) reorganized as $h(1+d/h)$; d and h are the depth of the rigid bed from the slope base and the slope height, respectively, as shown in Fig. 1a.

Further, the horizontal (a_h) and the vertical (a_v) seismic accelerations induced in the medium can be obtained from Eq. (5a, 5b) by differentiating Eq. (2a, 2b) twice with respect to time (t)

$$a_h(z,t) = \frac{k_h g}{C_s^2 + S_s^2}\left[(C_s C_{sz} + S_s S_{sz})\cos(\omega t) + (S_s C_{sz} - C_s S_{sz})\sin(\omega t)\right] \tag{5a}$$

$$a_v(z,t) = \frac{k_v g}{C_p^2 + S_p^2}\left[(C_p C_{pz} + S_p S_{pz})\cos(\omega t) + (S_p C_{pz} - C_p S_{pz})\sin(\omega t)\right], \tag{5b}$$

where $k_h g = -\omega^2 u_{h0}$ and $k_v g = -\omega^2 u_{v0}$, and k_h and k_v are the seismic acceleration coefficients along the horizontal and the vertical directions, respectively.

It is worth mentioning that such a spatial distribution in horizontal and vertical acceleration profiles can be reasonably assumed to be constant across an infinitesimally small rock mass element at a specific time, as shown in Fig. 1b (Santhoshkumar et al. 2019; Nandi et al. 2021b).

3.2 Generalized Hoek–Brown Criterion

Among different non-linear strength criteria, the GHB criterion (Hoek et al. 2002) is broadly recognized to delineate the inherent non-linearity in the rock mass strength. According to the GHB criterion, the fundamental expression for the pressure-dependent strength characteristics of a uniformly jointed rock mass system in two-dimensional principal stress (σ_1-σ_3) space can be written as

$$\frac{\sigma_1 - \sigma_3}{\sigma_{ci}} = \left(m_b \frac{\sigma_3}{\sigma_{ci}} + s \right)^a, \tag{6}$$

where σ_1 and σ_3 are the major and the minor principal stresses, respectively; a, m_b, and s are the dimensionless material parameters determined by the *GSI*.

It is worth noting that the *GSI* directly represents the rock mass quality by consuming a typical range from 10 for extremely poor rock masses to 100 for intact rocks. Based on the definition provided by Hoek et al. (2002), the dimensionless Hoek–Brown strength parameters (a, m_b, and s) can be presented as

$$a = \frac{1}{2} + \frac{1}{6}\left\{ e^{\left(-\frac{GSI}{15}\right)} - e^{\left(-\frac{20}{3}\right)} \right\} \tag{7a}$$

$$m_b = m_i e^{\left(\frac{GSI-100}{28-14D}\right)} \tag{7b}$$

$$s = e^{\left(\frac{GSI-100}{9-3D}\right)}, \tag{7c}$$

where m_i denotes the hardness of the rock, which usually ranges from 5 to 35, and D is the disturbance factor varying from 0 for the undisturbed state to 1 for the fully disturbed/fractured state of the rock mass. The work of Hoek and Brown (1997) can be referred to for further details about the assessment of *GSI*, m_i, and σ_{ci}.

By utilizing the concept of the Mohr stress circle, a subsequent modification in the GHB criterion (Eq. (6)) can be expressed as

$$\frac{R}{\beta_a}\left(1 + (1-a)\left(\frac{R}{\beta_a}\right)^k \right) = \frac{p}{\beta_a} + \zeta_a, \tag{8}$$

where $p = (\sigma_1 + \sigma_3)/2$ and $R = (\sigma_1 - \sigma_3)/2$ represent the average stress and the radius of the Mohr circle, respectively, and

$$\beta_a = A_a \sigma_{ci}; \quad \zeta_a = \frac{s}{m_b A_a}; \quad k = \frac{1-a}{a}; \quad A_a^k = \frac{m_b(1-a)}{2^{\frac{1}{a}}}, \tag{9}$$

Considering the GHB parameters (*GSI*, m_i, σ_{ci}, and D) as input, all the terms mentioned in Eq. (9) can ultimately be known for the subsequent analysis.

3.3 Method of Stress Characteristics

The MSC is a classical method to solve various plasticity problems in geotechnical engineering (Sokolovski 1960). It was later extended and applied to the domain of rock mechanics by different researchers (Serrano and Olalla 1994; Serrano et al. 2000; Keshavarz et al. 2016; Keshavarz and Kumar 2018, 2021). In this method, the equilibrium and the yield equations are simultaneously utilized to establish a system of hyperbolic partial differential equations subjected to physical boundary conditions (Veiskarami et al. 2014). Thus, the system of equations can be solved by any suitable numerical scheme, preferably by the finite-difference method (Sokolovski 1960; Jahanandish and Keshavarz 2005; Keshavarz et al. 2016; Keshavarz and Kumar 2021). A comprehensive discussion on the MSC and the solution procedure is available in the previous studies (Sokolovski 1960; Jahanandish and Keshavarz 2005; Keshavarz et al. 2016). However, this paper discusses a brief outline of the method for wholeness.

3.3.1 Equilibrium-Yield Equations

Figure 1a portrays the 2D plane strain representation of the proposed rock slope in the x–z plane with the slope crest O as the origin of the coordinate system. From Fig. 1b, the governing equations of the static equilibrium under the plane strain condition can be written as

$$\frac{\partial \sigma_x}{\partial x} + \frac{\partial \tau_{xz}}{\partial z} = X \tag{10a}$$

$$\frac{\partial \tau_{xz}}{\partial x} + \frac{\partial \sigma_z}{\partial z} = Z, \tag{10b}$$

where σ_x, σ_z, and τ_{xz} are the stress components acting upon an infinitesimally small rock mass element (Fig. 1b); X and Z are the body forces per unit volume of the rock mass in x- and z-directions, respectively, and can be expressed as

$$X = -\gamma \alpha_h \tag{11a}$$

$$Z = \gamma\left(1 \pm \alpha_v\right), \tag{11b}$$

where γ is the unit weight of the rock mass, and α_h and α_v are the non-dimensional horizontal and vertical accelerations, respectively, which can be written as $\alpha_h = a_h/g$ and $\alpha_v = a_v/g$. It is worth mentioning that the directions of the horizontal and the vertical accelerations are chosen to replicate the most critical seismic inertial impact in the analysis (Santhoshkumar et al. 2019; Nandi et al. 2021b). A separate parametric study is reported in this paper later by considering this aspect.

By following the recommendations of Booker and Davis (1972), the generalized yield criterion for a homogeneous medium can be written as a function of the aforesaid stress components in Eq. (12)

$$f\left(\sigma_x, \sigma_z, \tau_{xz}\right) = R - F(p, \theta) = 0, \tag{12}$$

where θ represents the orientation of the major principal stress (σ_1) about the positive z-axis with a counter-clockwise sense of rotation taken as positive.

From the Mohr circle, the stress components can also be derived as

$$\sigma_x = p - R\cos 2\theta \tag{13a}$$

$$\sigma_z = p + R\cos 2\theta \tag{13b}$$

$$\tau_{xz} = R\sin 2\theta. \tag{13c}$$

Simultaneous utilization of the equilibrium equations given in Eq. (10a, 10b) and the yield equations given in Eq. (13a, 13b, 13c), followed by some algebraic simplifications, establishes two families of characteristics. The equilibrium equations along the characteristics can be termed the equilibrium-yield equations (Jahanandish and Keshavarz 2005; Keshavarz and Kumar 2018, 2021) and are written as
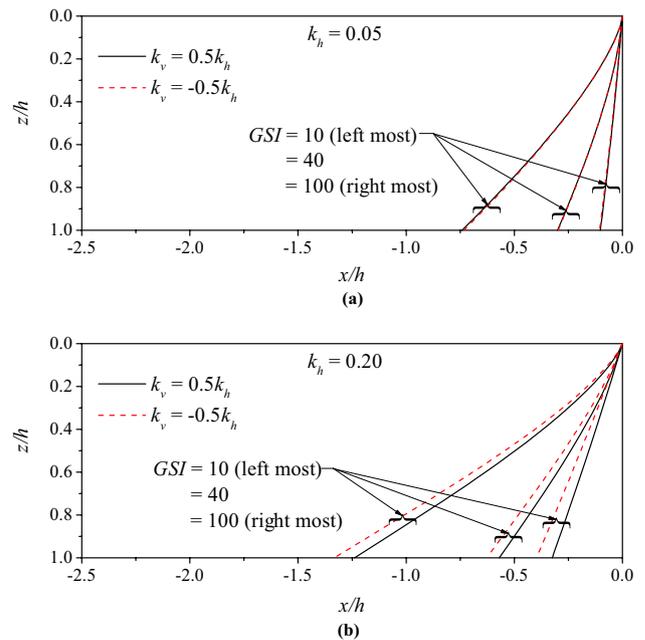
along σ^- direction

Fig. 2 Effect of k_v direction on LSFs for different values of *GSI* with $\sigma_{ci}/\gamma h = 8$, $m_i = 15$, $D = 0$, $\xi = 0.10$, $\omega H/V_s = 0.94$, $V_p/V_s = 1.87$, and $d/h = 0$: **a** $k_h = 0.05$; **b** $k_h = 0.20$

$$m = 0; \quad \mu = \frac{1}{2}\cos^{-1}\left(\frac{1}{1 + (1 - a)\left(\frac{R}{\beta_a}\right)^k(1 + k)}\right). \tag{16}$$

$$\left.\begin{array}{l} \frac{dx}{dz} = \tan(\theta - m - \mu) \\ \sin 2(m - \mu)dp + 2Fd\theta = -\cos 2m[\{\sin 2\mu dx - \cos 2\mu dz\}X + \{\cos 2\mu dx + \sin 2\mu dz\}Z] \end{array}\right\} \tag{14a}$$

along σ^+ direction

$$\left.\begin{array}{l} \frac{dx}{dz} = \tan(\theta - m + \mu) \\ \sin 2(m + \mu)dp + 2Fd\theta = \cos 2m[\{\sin 2\mu dx + \cos 2\mu dz\}X - \{\cos 2\mu dx - \sin 2\mu dz\}Z] \end{array}\right\}, \tag{14b}$$

where

$$\tan 2m = \frac{1}{2F}\frac{\partial F}{\partial \theta}; \quad \cos 2\mu = \cos 2m\frac{\partial F}{\partial p}. \tag{15}$$

For the GHB criterion, the values of m and μ can be determined as

In addition, the concept of the instantaneous friction angle (ρ), as proposed by Serrano and Olalla (1994), is presented in Eq. (17) along with a graphical illustration in Fig. 1c

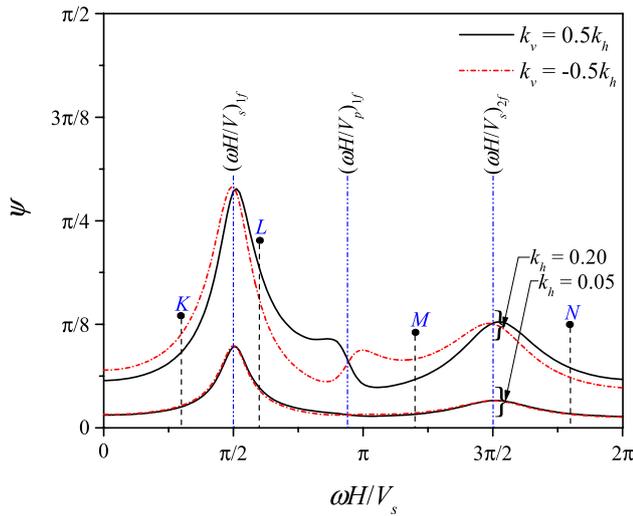$$\frac{\partial R}{\partial p} = \sin \rho. \tag{17}$$

Fig. 3 Effect of k_v direction on ψ for different values of k_h and $\omega H/V_s$ with $\sigma_{ci}/\gamma h = 8$, $GSI = 40$, $m_i = 15$, $D = 0$, $\xi = 0.10$, $V_p/V_s = 1.87$, and $d/h = 0$
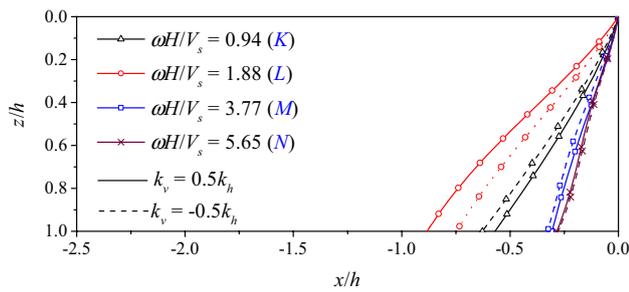

Fig. 4 Effect of k_v direction on LSFs for different values of $\omega H/V_s$ with $\sigma_{ci}/\gamma h = 8$, $GSI = 40$, $m_i = 15$, $D = 0$, $\xi = 0.10$, $k_h = 0.20$, $V_p/V_s = 1.87$, and $d/h = 0$

Subsequent utilization of the concept of the instantaneous friction angle defined in Eq. (17) along with Eq. (8) further assists in defining the following modified expressions for R and p as given in Eq. (18a, 18b):

$$R = \beta_a \left(\frac{1 - \sin \rho}{k \sin \rho} \right)^{\frac{1}{k}} \tag{18a}$$

$$p = \beta_a \left[\left\{ a \left(\frac{1 + k \sin \rho}{\sin \rho} \right) \left(\frac{1 - \sin \rho}{k \sin \rho} \right)^{\frac{1}{k}} \right\} - \zeta_a \right]. \tag{18b}$$

3.3.2 Boundary Conditions

For the current 2D slope stability problem, the known boundaries include (i) the top surface (OG) of the slope
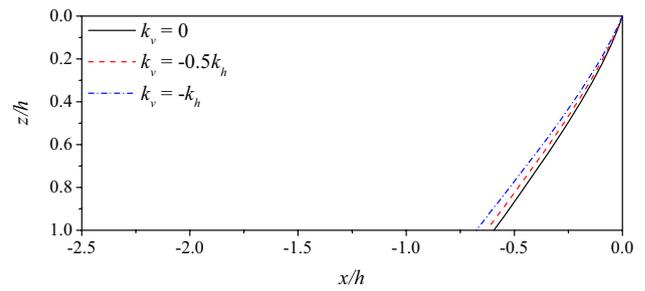
Fig. 5 Variation of LSFs for different values of k_v with $\sigma_{ci}/\gamma h = 8$, $GSI = 40$, $m_i = 15$, $D = 0$, $\xi = 0.10$, $k_h = 0.2$, $\omega H/V_s = 0.94$, $V_p/V_s = 1.87$, and $d/h = 0$

and (ii) the slope face (OA). Since a uniformly distributed surcharge (q) acts along OG, the normal (σ_{ng}) and shear (τ_g) stresses developed along OG under seismic conditions can be expressed as

$$\sigma_{ng} = q \left(1 \pm \alpha_v \right) \tag{19a}$$

$$\tau_g = -q \alpha_h. \tag{19b}$$

From the concept of the Mohr stress circle, it can be obtained as

$$R_g = \sqrt{\left(\sigma_{ng} - p_g \right)^2 + \tau_g^2}, \tag{20}$$

where p_g and R_g denote the magnitude of p and R, respectively, along OG.

Subsequently, on substitution of Eqs. (19a, 19b) and (20) into Eq. (8), the average stress (p_g) on OG can be determined by solving the following non-linear equation numerically:

$$\frac{\sqrt{\left(\sigma_{ng} - p_g \right)^2 + \tau_g^2}}{\beta_a} \left(1 + (1 - a) \left(\frac{\sqrt{\left(\sigma_{ng} - p_g \right)^2 + \tau_g^2}}{\beta_a} \right)^k \right) = \frac{p_g}{\beta_a} + \zeta_a. \tag{21}$$

Once p_g is obtained, the major principal stress orientation (θ_g) along OG can be simply evaluated using Eq. (22). However, Eq. (13b, 13c), along with the necessary stress boundary conditions applicable to the OG plane, needs to be employed to obtain Eq. (22)

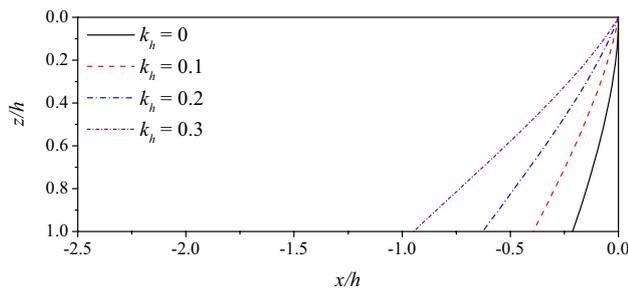$$\theta_g = -\frac{1}{2} \left(\delta + \sin^{-1} \left(\frac{p_g \sin \delta}{R_g} \right) \right), \tag{22}$$

where

$$\delta = \tan^{-1} \left(\frac{\alpha_h}{1 \pm \alpha_v} \right) \leq \rho_g, \tag{23}$$

and ρ_g is the instantaneous friction angle along OG.

Table 1 Input parameters used in the analysis

Parameters	Range
$\sigma_{ci}/\gamma h$	0.625–40
GSI	10–100
m_i	5–35
D	0–1.0
ξ	0.05–0.15
k_h	0–0.3
k_v	$(-k_h) - (+0.5k_h)$
$\omega H/V_s$	0–2π
$\omega H/V_p$	0–1.1π
d/h	0–1.0

Fig. 6 Variation of LSFs for different values of k_h with $\sigma_{ci}/\gamma h = 8$, $GSI = 40$, $m_i = 15$, $D = 0$, $\xi = 0.10$, $k_v = -0.5k_h$, $\omega H/V_s = 0.94$, $V_p/V_s = 1.87$, and $d/h = 0$

In contrast, being a stress-free surface, the limiting slope face (OA) implies that the normal and the shear stresses along OA become zero. It further indicates that $R_s = p_s$, where p_s and R_s represent the magnitude of p and R, respectively, along the stress-free slope face (OA). Hence, similar to p_g, the average stress (p_s) on OA can be calculated numerically by solving Eq. (24)

$$\frac{p_s}{\beta_a}\left(1 + (1-a)\left(\frac{p_s}{\beta_a}\right)^k\right) = \frac{p_s}{\beta_a} + \zeta_a. \tag{24}$$

In addition to the stress-free boundary condition, the condition given in Eq. (25) must also be fulfilled at each point on OA

$$\frac{dx}{dz} = \tan\theta_s, \tag{25}$$

where θ_s is the orientation of the major principal stress along OA.

3.4 Determination of Limiting Slope Face

Due to two distinct states of stress at the slope crest (O), as evident from Eqs. (21) and (24), there exists a stress

singularity at point O. Such a stress singularity produces a null length σ^- characteristic in the neighborhood of O, which in turn leads to the following modification of Eq. (14a)

$$-\sin 2\mu \, dp + 2Rd\theta = 0. \tag{26}$$

Further, the stress singularity corroborates a rotation in the major principal stress orientation, which can be quantified by establishing the major principal stress direction at point O but along OA (ψ), as given in Eq. (27). Equation (26) needs to be integrated from the top surface (OG) to the slope face (OA) in conjunction with Eq. (18a, 18b) to achieve Eq. (27)

$$\psi = \theta_g + \frac{1}{2k}\left(\cot\rho_s - \cot\rho_g + \ln\left(\frac{\tan(0.5\rho_g)}{\tan(0.5\rho_s)}\right)\right), \tag{27}$$

where ρ_s is the instantaneous friction angle along OA.

Subsequently, the LSF (OA) is traced through the construction of a stress characteristic network by gradually emanating from the known boundary (OG) to the unknown boundary (OA). The formation of such stress characteristics network is often established by adopting a suitable finite-difference scheme for Eq. (14a, 14b), as reported by previous researchers (Jahanandish and Keshavarz 2005; Keshavarz et al. 2016). However, to avoid numerical instability in the simulation process, a minimum surcharge (q) is considered in the analysis while generating the stress characteristics network (Sokolovski 1960; Nandi et al. 2021a, b). Based on the recommendation of Srikar and Mittal (2020), the selected surcharge should not interfere with the amplification of seismic waves as ensued from the MPD approach.

4 Results and Discussion

The stability of the rock slope was established under the unified framework of the GHB criterion, the MSC, and the MPD approach by developing an in-house computer code in MATLAB. Accordingly, the results manifesting the condition of the limiting stability (FS = 1.0) are presented as LSF. Under seismic conditions, the magnitude of θ at the slope crest (O) but along OA, defined by ψ in Eq. (27), plays a decisive role in shaping the LSF. Hence, a series of computations corresponding to various t/T values ranging from 0 to 1 is performed to ensure the maximum ψ at O. Eventually, the developed LSF serves as an efficient, inexpensive, and safe design guideline for the stability analysis of slopes as discoursed by Nandi et al. (2021b). An elaborative parametric study is performed in this study to envisage such limiting behavior of rock slopes. A practical range of input parameters is adopted from various studies available in the literature (Li et al. 2009; Jiang et al. 2016; Sarkar and Chakraborty
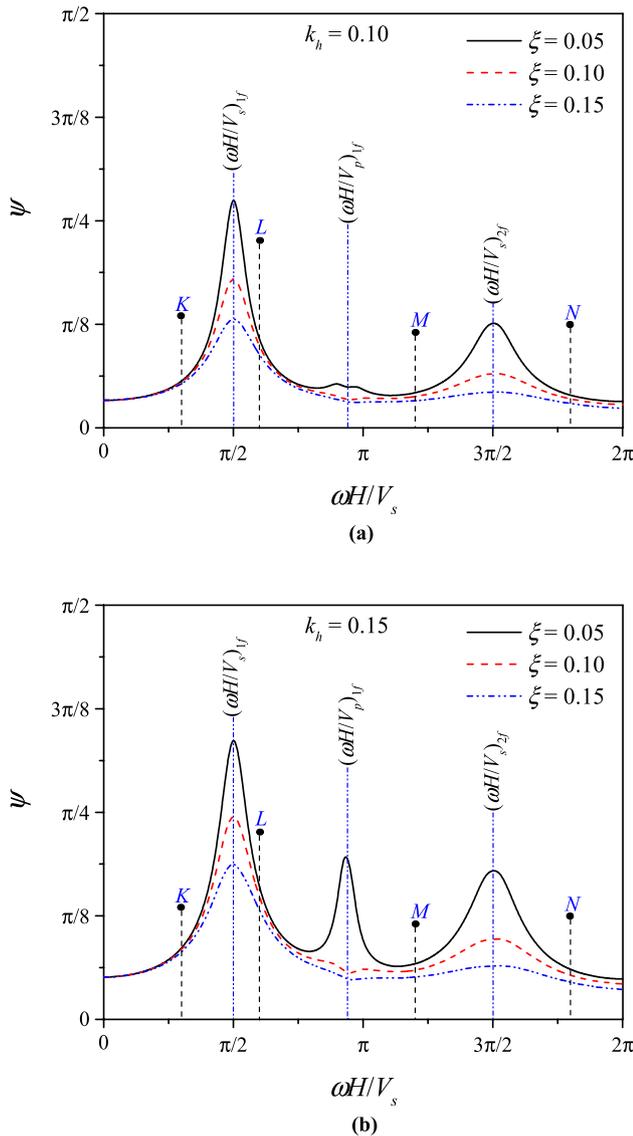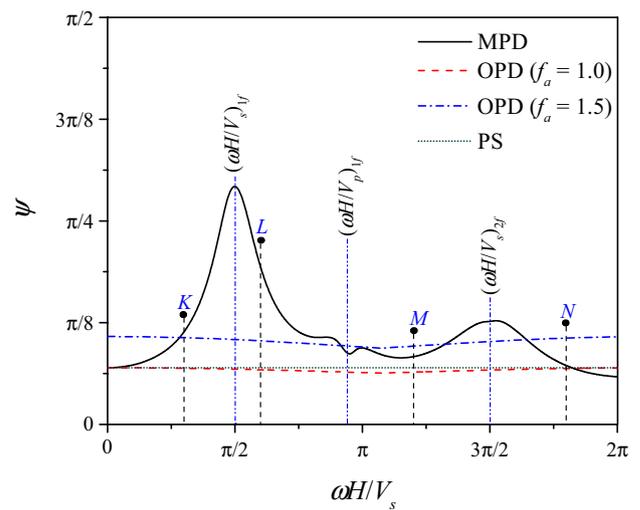
(a)

Fig. 8 Variation of ψ for different seismic approaches with $\sigma_{ci}/\gamma h = 8$, $GSI = 40$, $m_i = 15$, $D = 0$, $\xi = 0.10$, $k_h = 0.2$, $k_v = \pm 0.5k_h$, $V_p/V_s = 1.87$, and $d/h = 0$

(b)

Fig. 7 Variation of ψ for different values of ξ and $\omega H/V_s$ with $\sigma_{ci}/\gamma h = 8$, $GSI = 40$, $m_i = 15$, $D = 0$, $k_v = \pm 0.5k_h$, $V_p/V_s = 1.87$, and $d/h = 0$: **a** $k_h = 0.10$; **b** $k_h = 0.15$

2021; Zhong and Yang 2021) and mentioned in Table 1. It is worth noting from Eq. (25) that the variation in θ_s primarily governs the LSF; hence, ψ is additionally chosen to quantify the current outcome.

4.1 Effect of Seismic Accelerations

Under seismic conditions, both horizontal and vertical seismic accelerations prompt the failure of rock slopes (Sun et al. 2012; Jiang et al. 2016; Qin and Chian 2018; Zhao et al. 2017, 2020). However, the effect of vertical acceleration is often overlooked while performing the seismic stability

analysis of rock slopes. In the most critical situation, the horizontal seismic acceleration is expected to act in the negative x-direction, that is, away from the slope, as shown in Fig. 1a (Li et al. 2009; Nandi et al. 2021b). Conversely, the critical direction of vertical acceleration cannot be simply established as it depends on various factors, such as the level of seismicity (Jiang et al. 2016), the frequency content of seismic waves (Nandi et al. 2021b), and the rock mass quality (Jiang et al. 2016). Hence, to unveil a trend of the functional dependency of k_v on the above-mentioned parameters, an imperative study is presented in Figs. 2, 3, 4 considering both positive (downward) and negative (upward) directions of k_v with a magnitude of $0.5k_h$. Figure 2 presents the effect of the direction of k_v on the behavior of the LSF for different values of GSI and k_h. It can be seen from Fig. 2 that the influence of the direction of k_v is inconsequential at the lower seismicity level. However, as the seismicity level escalates with increasing k_h, a remarkable deviation in the LSFs can be observed due to the direction change of k_v. The magnitudes and directions of k_v affect both driving and resisting forces operating on the derived critical slip surface (CSS), which dictate the limiting stability of the rock slope (Jiang et al. 2016).

It can be further noticed from Fig. 2 that the upward direction of k_v demands a flat LSF at $\omega H/V_s = 0.94$. However, such observation may not be true for other values of $\omega H/V_s$. Hence, the influence of the frequency-dependent behavior of k_v on ψ is presented in Fig. 3 by selecting four pertinent points (K, L, M, and N) corresponding to $\omega H/V_s = 0.94$, 1.88, 3.77, and 5.65, respectively. The points K, L, M, and N encompassing the currently adopted frequency range assist
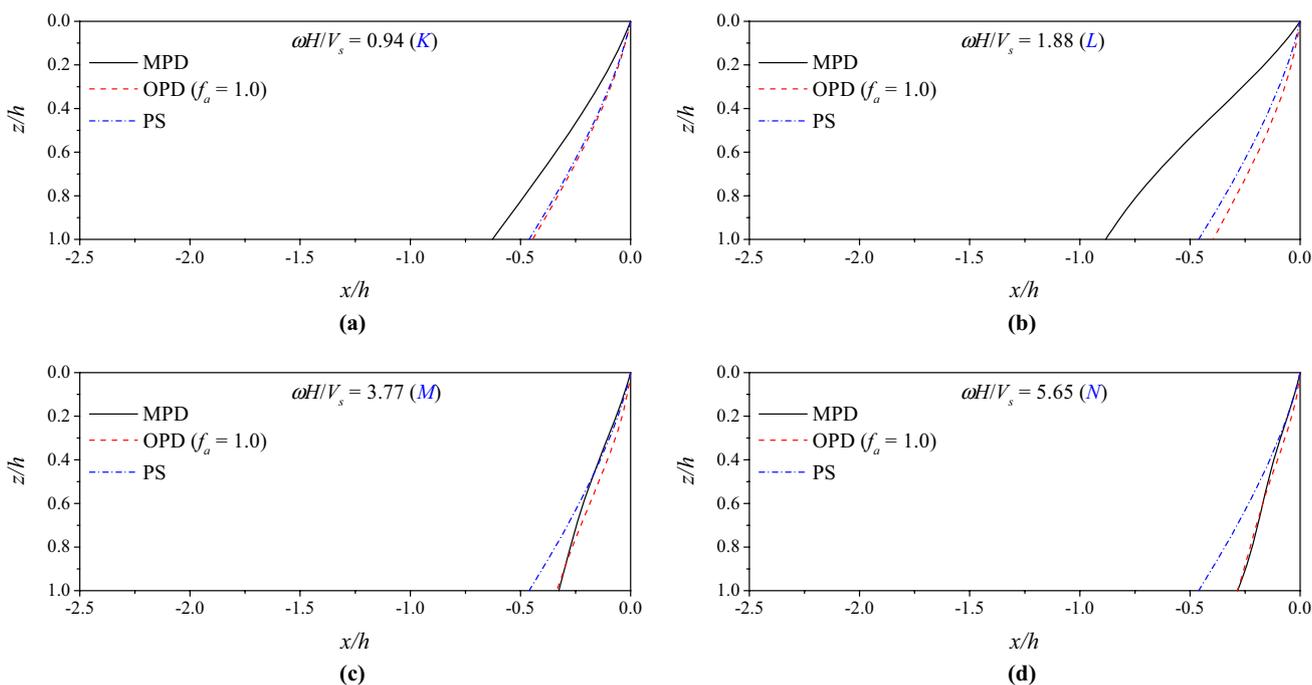
Fig. 9 Variation of LSFs for different seismic approaches with $\sigma_{ci}/\gamma h = 8$, $GSI = 40$, $m_i = 15$, $D = 0$, $\xi = 0.10$, $k_h = 0.2$, $k_v = \pm 0.5 k_h$, $V_p/V_s = 1.87$, and $d/h = 0$: **a** $\omega H/V_s = 0.94$; **b** $\omega H/V_s = 1.88$; **c** $\omega H/V_s = 3.77$; **d** $\omega H/V_s = 5.65$

in portraying the frequency-dependent behavior of the LSF effectively. The points K and L are chosen to bracket the first fundamental frequency of S-waves. Similarly, points M and N are selected to bracket the second fundamental frequency of S-waves. Consequently, the first fundamental frequency of P-waves gets bracketed inevitably by the points L and M. By following the recommendation of Kramer (1996), the $(n+1)$th normalized fundamental frequency of S-waves propagating through a dry, homogeneous, and damped rock mass can be expressed as

$$\left(\frac{\omega H}{V_s}\right)_{(n+1)f} = \frac{\pi}{2} + n\pi \; ; [n = 0, 1, 2, \ldots\ldots\ldots\ldots, \infty].$$
(28)

In Fig. 4, the LSFs derived at different values of $\omega H/V_s$ corresponding to the aforesaid points K, L, M, and N are presented for $k_h = 0.2$. It can be seen from Figs. 3 and 4 that the variations of ψ and LSF are significantly affected by the direction of k_v depending on the frequency content of seismic waves. For higher values of k_h, the upward direction of k_v is seen to be critical for a range of $\omega H/V_s$ varying from 0 to $\pi/2$ (Fig. 3), whereas the downward direction of k_v seems to be critical for $\omega H/V_s$ varying from $\pi/2$ to 0.93π. It is worth noting that $\omega H/V_s = \pi/2$ and $\omega H/V_s = 0.93\pi$ represent the first normalized fundamental frequencies of S- and

P-waves $((\omega H/V_s)_{1f}$ and $(\omega H/V_p)_{1f})$, respectively, considering $V_p/V_s = 1.87$ as applicable to most geo-materials (Kramer 1996). Hence, it is reasonable to infer that the critical direction of k_v alters with the fundamental frequency of seismic waves. It can be seen from Fig. 4 that the difference in the LSFs derived for the upward and the downward directions of k_v reduces with the increase in $\omega H/V_s$ beyond $\pi/2$. Moreover, the LSFs become steeper as the frequency passes through the points L, M, and N. It may be attributed to the fact that the amplified acceleration profile in the horizontal direction undergoes a phase shift at points L, M, and N, which eventually subsides the net seismic inertial force in the medium significantly. Hence, it can be conceived that vertical seismic acceleration certainly needs meticulous attention while considering the seismic stability analysis of slopes. By considering the set of parameters adopted for the current parametric study, the upward direction of k_v is typically found to be critical. Accordingly, it is followed in the subsequent analysis.

The variations of the LSF for different magnitudes of k_v and k_h are shown in Figs. 5 and 6, respectively. It can be observed that the LSFs become progressively flat with an increase in k_v and k_h. However, the extent of variation in the LSFs with different k_h values is quite significant compared to k_v. It may be attributed to the increase in k_h expedites greater seismic inertial forces in the medium than k_v.
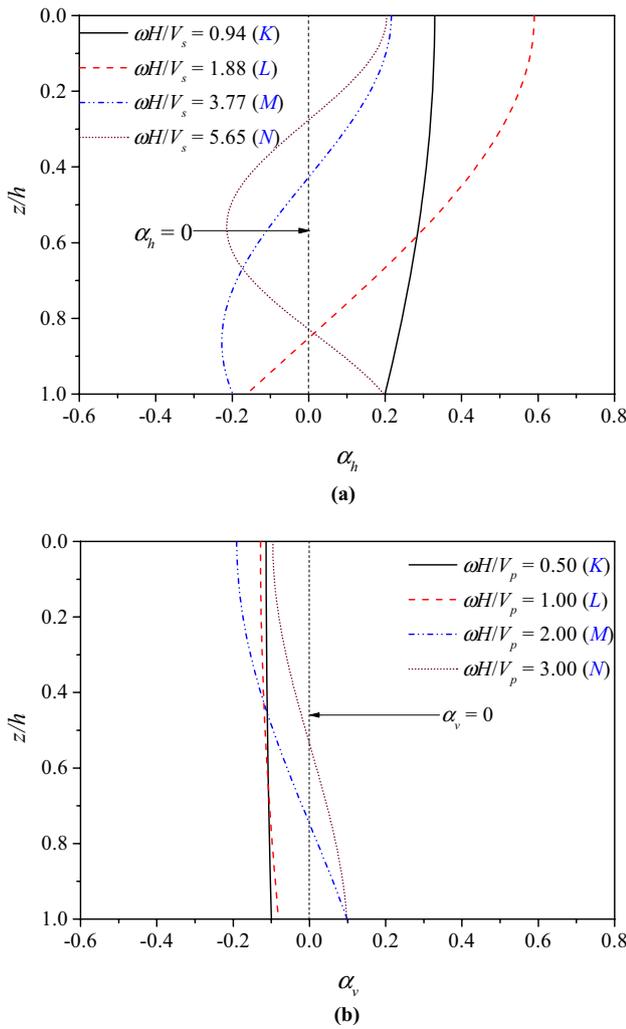
Fig. 10 Variation of **a** α_h for different values of $\omega H/V_s$; **b** α_v for different values of $\omega H/V_p$; with $\sigma_{ci}/\gamma h = 8$, $GSI = 40$, $m_i = 15$, $D = 0$, $\xi = 0.10$, $k_h = 0.2$, $k_v = \pm 0.5 k_h$, $V_p/V_s = 1.87$, and $d/h = 0$

4.2 Effect of Rock Mass Damping

The attenuation response in the seismic impact caused by the rock mass damping (ξ), especially near the fundamental frequencies of seismic waves, is worth exploring. In Fig. 7, the variation of ψ with various magnitudes of ξ and k_h is shown. From Fig. 7, a sudden rise in the magnitude of ψ at the fundamental frequencies of seismic waves can be observed due to the resonance effect. However, such resonance effect is found to diminish with the increase in ξ. For $k_h = 0.1$, a reduction of 5.42%, 16.85%, 21.29%, and 25.60% can be noted in the magnitude of ψ at the points K, L, M, and N, respectively, with an increase in ξ from 5 to 15%. Hence, it can be perceived that the damping affects the response at higher frequencies more than at lower frequencies (Kramer 1996).

4.3 Effect of Frequency

Figure 8 presents the variation of ψ with $\omega H/V_s$ for different seismic approaches (MPD, OPD, and PS). It can be seen from Fig. 8 that the MPD approach generates distinct peaks in the variation of ψ at the fundamental frequencies of S-waves. In contrast, the OPD approach shows a mild variation in the magnitude of ψ even at higher values of f_a, whereas the value of ψ obtained from the PS approach is independent of the frequencies for the apparent reason. For different seismic approaches, the variation of LSFs at different frequency contents corresponding to the points K, L, M, and N is presented in Fig. 9. It can be conceived from Fig. 9 that considerably steeper LSFs derived from the OPD and the PS approaches severely overestimate the limiting stability of the rock slope compared to the MPD approach at the frequency levels corresponding to K and L. In contrast, for the frequency contents corresponding to M and N, the PS approach develops a relatively flat LSF compared to the MPD approach and thus resulting in an over-conservative design, especially at the higher frequency level. The diverse trends of ψ and LSF with $\omega H/V_s$ for different seismic approaches can be understood well by plotting the distributions of α_h and α_v along the slope height, as shown in Fig. 10. It can be observed from Fig. 10 that the resulting amplified acceleration profiles encounter a usual phase change at each fundamental frequency ($\pi/2$, $3\pi/2$) of the respective seismic wave, which dives into a subsequent phase shift in the seismic forces induced in the medium (Nandi et al. 2021b). Eventually, the seismic inertia forces predicted by the MPD approach become an obvious function of $\omega H/V_s$ and ξ, which cannot be captured by the OPD or the PS approach due to inherent limitations. Thus, the MPD approach contributes to a more rational seismic design of rock slopes by urging for the effective inclusion of the frequency content, the rock mass damping, and the wave velocities.

4.4 Effect of the Depth of Rigid Base

The depth of the rigid base (H), as shown in Fig. 1a, may not be a constant parameter. It may, instead, vary depending on the actual geological formation of the deposit. Figure 11 shows the variation of LSFs for different values of d/h ratio at various frequency levels. It can be seen from Fig. 11 that the effect of the d/h ratio on the LSF is not notable up to a certain critical depth from the top surface (OG) of the slope. However, different LSFs at various d/h ratios can be observed beyond the aforesaid critical depth. Figure 11 shows that the range of such critical depth is hugely dependent on the frequency level. At a relatively low value
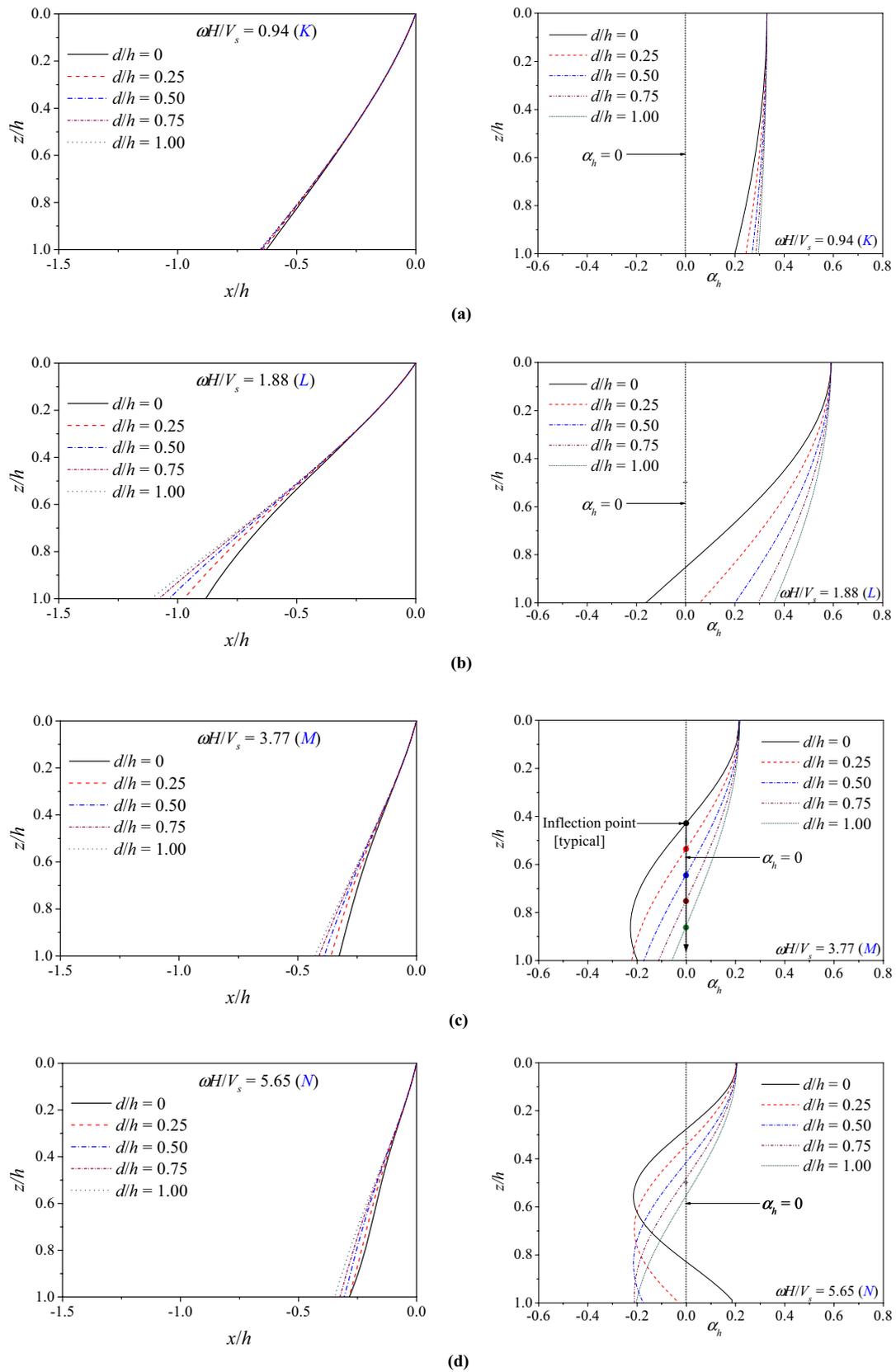
Fig. 11 Variation of LSFs and α_h for different values of d/h with $\sigma_{ci}/\gamma h = 8$, $GSI = 40$, $m_i = 15$, $D = 0$, $\xi = 0.10$, $k_h = 0.2$, $k_v = \pm 0.5 k_h$, and $V_p/V_s = 1.87$: **a** $\omega H/V_s = 0.94$; **b** $\omega H/V_s = 1.88$; **c** $\omega H/V_s = 3.77$; **d** $\omega H/V_s = 5.65$
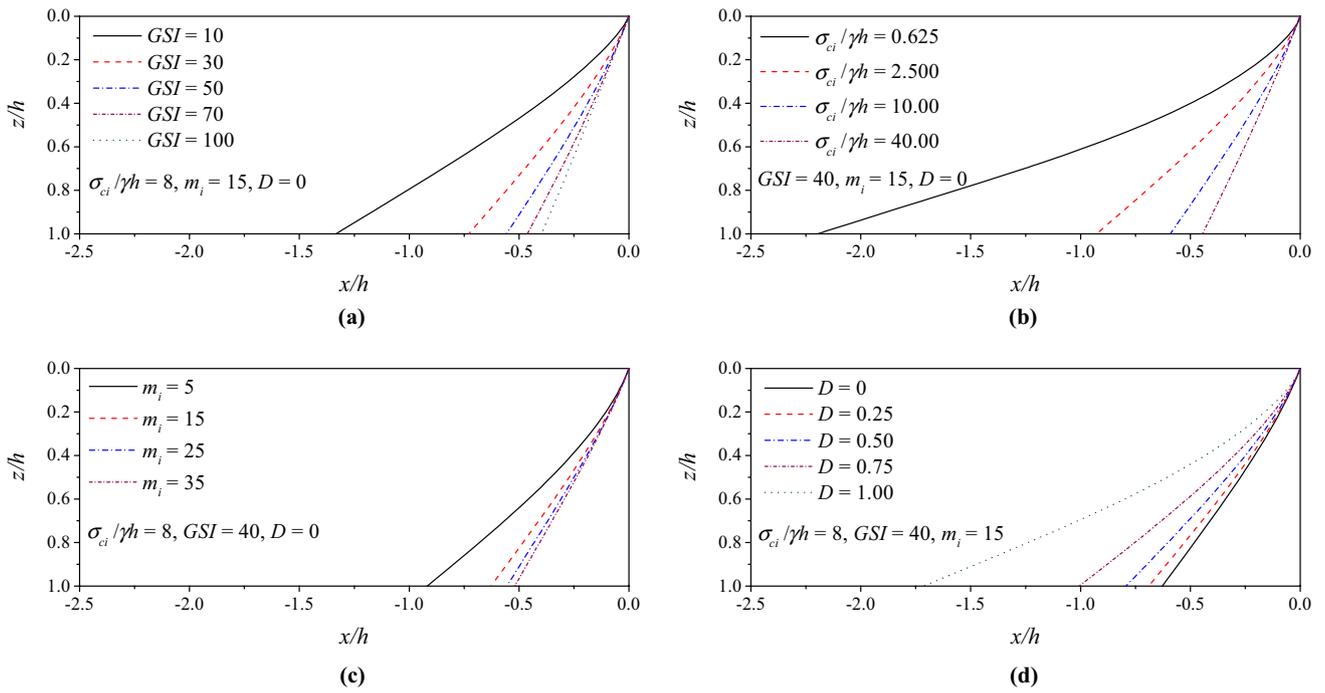
Fig. 12 Variation of LSFs with $\xi = 0.10$, $k_h = 0.2$, $k_v = -0.5k_h$, $\omega H/V_s = 0.94$, $V_p/V_s = 1.87$, and $d/h = 0$ for different values of: **a** *GSI*; **b** $\sigma_{ci}/\gamma h$; **c** m_i; **d** *D*
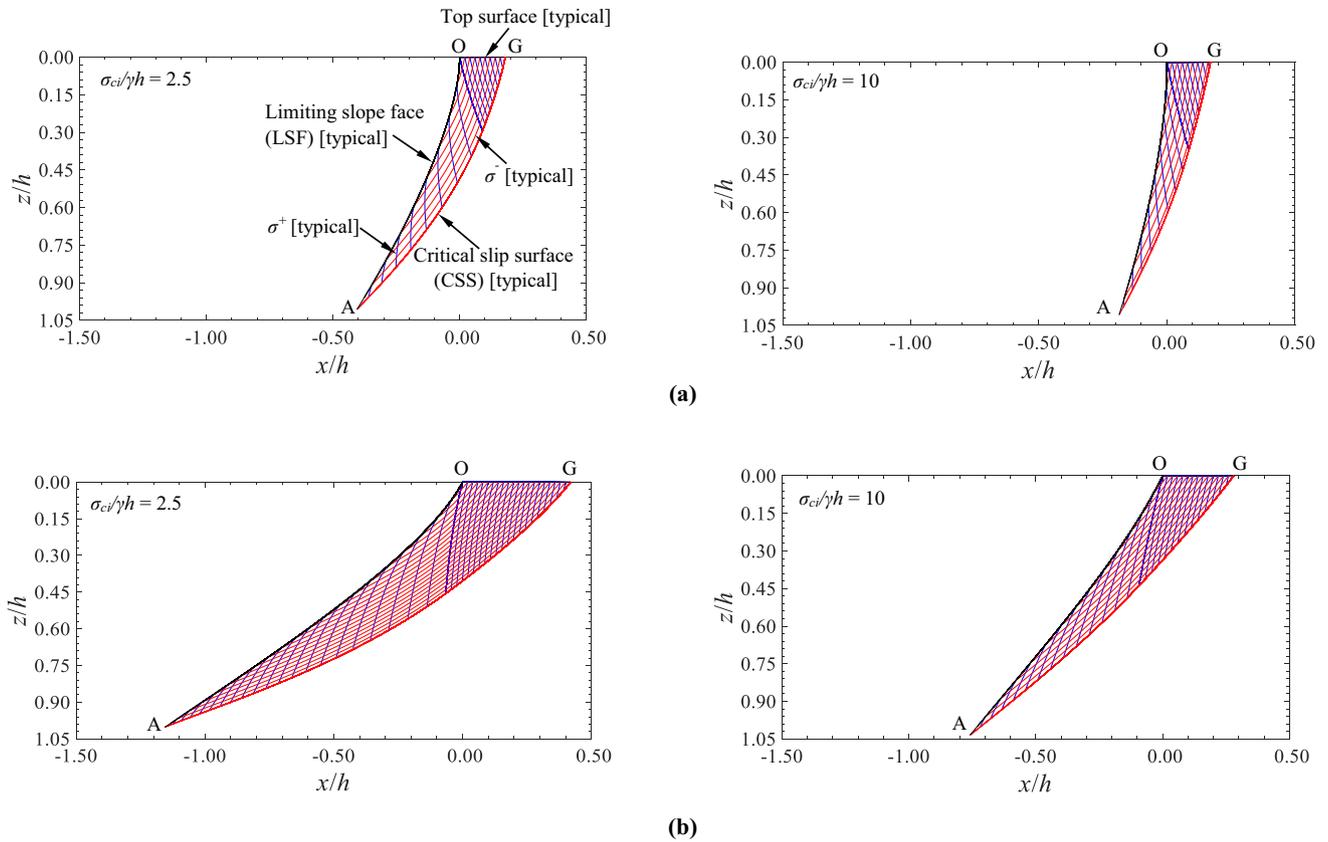
Fig. 13 Stress characteristics meshes for $GSI = 40$, $m_i = 15$, $D = 0$, $\xi = 0.10$, $k_v = -0.5k_h$, $\omega H/V_s = 0.94$, $V_p/V_s = 1.87$, and $d/h = 0$: **a** $k_h = 0$; **b** $k_h = 0.25$
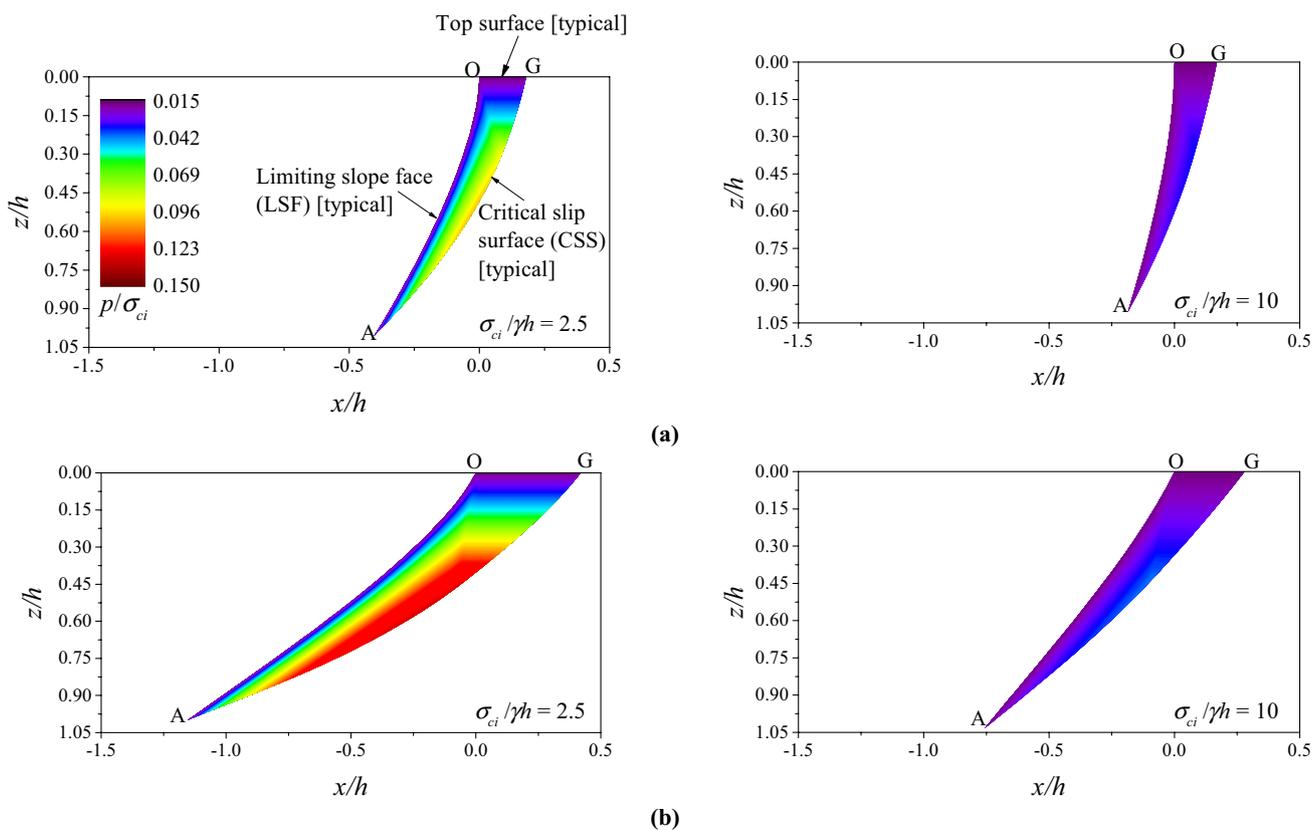
Fig. 14 Normalized stress (p/σ_{ci}) contours for $GSI = 40$, $m_i = 15$, $D = 0$, $\xi = 0.10$, $k_v = -0.5k_h$, $\omega H/V_s = 0.94$, $V_p/V_s = 1.87$, and $d/h = 0$: **a** $k_h = 0$; **b** $k_h = 0.25$

of $\omega H/V_s$ (point K), the critical depth almost extends to the entire height of the slope, and hence, the magnitude of the d/h ratio is seen to have no substantial impact on the LSF. In contrast, at the higher values of $\omega H/V_s$ (points L, M, and N), the critical depth does not stretch beyond $z/h = 0.3$. It can be further endorsed by plotting the normalized horizontal acceleration (α_h) profile committed along the depth of the rock slope, as shown in Fig. 11. In Fig. 11a, the fluctuation of α_h corresponding to the point K is not found to be significant with the variation of the d/h ratio. In contrast, a remarkable variety of α_h corresponding to higher frequency levels (points L, M, and N) can be observed with the increase in the d/h ratio (Fig. 11b–d). At frequencies corresponding to points L, M, and N, the inflection points responsible for the phase change in α_h shift to a deeper depth as d/h ratio increases, implying a consequent rise in the seismic inertia forces in the vibrating medium. Hence, it can be realized that increasing d/h ratio at higher frequency necessitates relatively flat LSFs beyond the critical depth to compensate for such enhanced inertia forces induced in the medium.

4.5 Effect of Rock Mass Properties

Figure 12 shows the variation of LSFs for different rock mass properties (*GSI*, $\sigma_{ci}/\gamma h$, m_i, and *D*) with $\xi = 0.10$, $k_h = 0.2$, $k_v = -0.5k_h$, $\omega H/V_s = 0.94$, $V_p/V_s = 1.87$, and $d/h = 0$. In Fig. 12a–c, the LSFs adopt steeper configurations with the enhancement in the magnitude of *GSI*, $\sigma_{ci}/\gamma h$, and m_i. It is worth mentioning that the enhancement in the value of *GSI*, $\sigma_{ci}/\gamma h$, and m_i generally indicates a good quality rock mass with relatively higher strength. In contrast, the strength of the rock mass deteriorates with an increase in the rock mass disturbance factor (*D*). Hence, the LSFs are found to acquire flat layouts with an increase in the magnitude of *D*.

4.6 Adaptive Slip Surface and Stress Contour

In Fig. 13, the variation of the CSSs alongside the LSFs is presented with different values of $\sigma_{ci}/\gamma h$ under static and seismic conditions. The evolved CSSs are found to be non-linear without following any specific shape, as assumed in the previous investigations. In addition, the extent of the influence zone at a given value of $\sigma_{ci}/\gamma h$ is found to expand

Fig. 15 **a** Problem definition for limiting slope profile (LSF) with an inclined top surface; **b** variation of LSFs based on PS approach for different values of χ with $\sigma_{ci}/\gamma h = 8$, $GSI = 40$, $m_i = 15$, $D = 0$, $k_v = -0.5k_h$

(a)

(b)
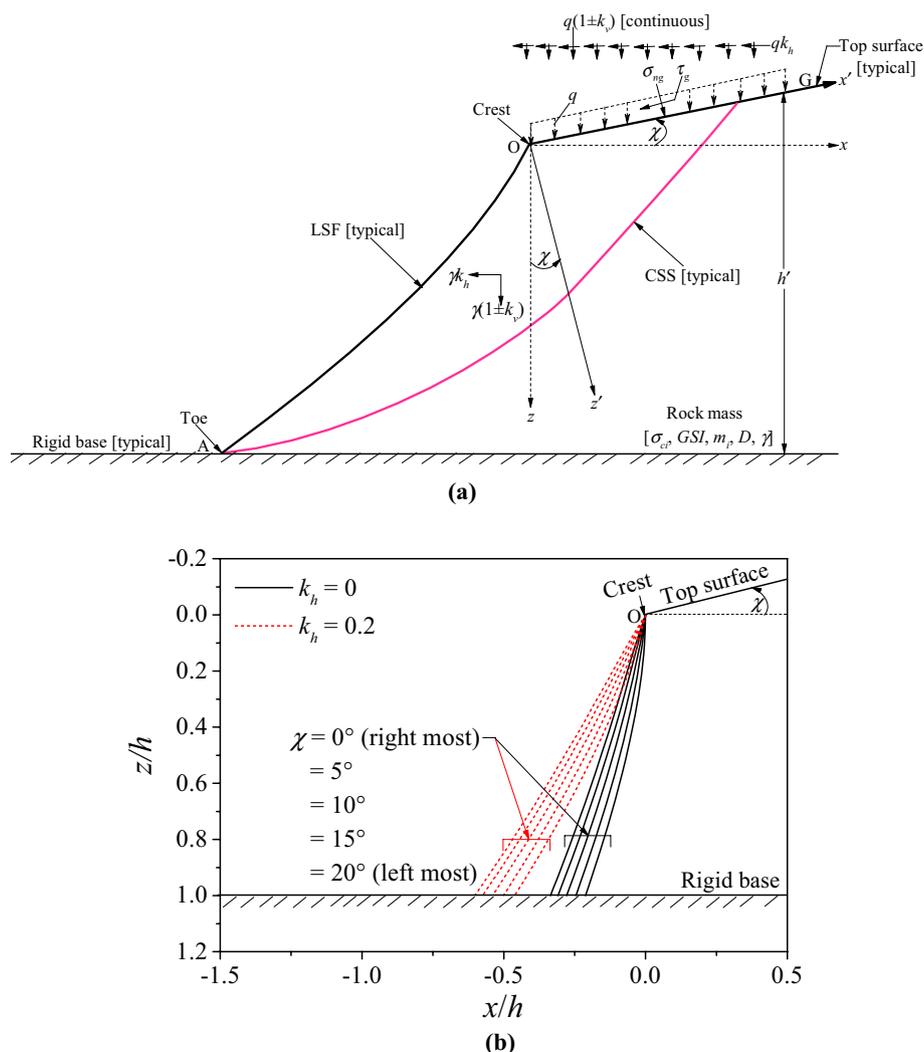
with increased seismic accelerations. However, the size and the curvature of the CSSs decrease with increasing $\sigma_{ci}/\gamma h$ to produce comparatively steeper LSFs. Such a self-adaptive feature of the CSS, along with the associated plastic failure domain, helps to perceive the seismic slope stability precisely. Further, this investigation ensures continuous monitoring of stresses mobilized in the developed failure domain. Figure 14 shows the mobilization of stresses inside the disturbed region as normalized stress (p/σ_{ci}) contours. With increasing seismicity levels, the stress contours at a lower value of $\sigma_{ci}/\gamma h$ reveal a relatively intense and rapid mobilization of stresses near the CSS but a gradual release toward the stress-free slope face. In contrast, a uniform and mild variation in the mobilized stresses can be noticed at a higher magnitude of $\sigma_{ci}/\gamma h$. Further, it can be seen from Fig. 14 that the normalized stress (p/σ_{ci}) drops significantly with an increase in the value of $\sigma_{ci}/\gamma h$.

4.7 Inclined Top Surface

In this study, LSFs are primarily derived assuming the horizontal top surface of the slope (OG) (Fig. 1a). However, on several occasions, the top surface of the slope (OG) may be inclined with the horizontal (χ), as shown in Fig. 15a. The present LSF concept is also applicable to address the seismic stability of slopes with an inclined top surface (OG). However, the current MPD approach demands a horizontal top surface to conduct the analysis (Gu and Wu 2019; Zhao et al. 2020; Zhong and Yang 2021). Hence, an attempt is made to derive the LSF with the inclined top surface by employing the PS approach. Consequently, the stress boundary conditions applicable to OG, as stated in Eq. (19a, 19b), can be modified as (Kumar and Mohan Rao 2003; Kumar and Chakraborty 2013)
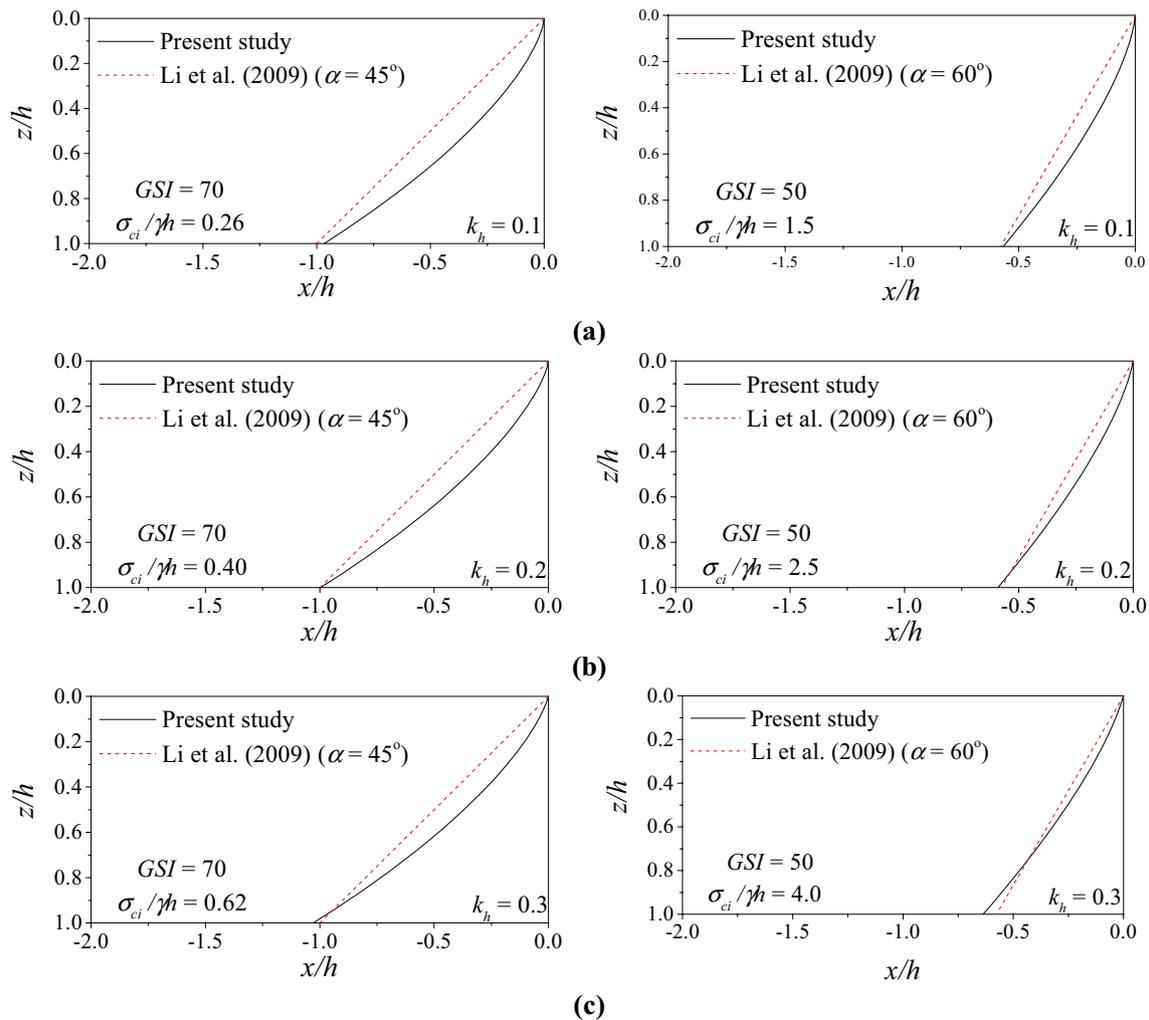
Fig. 16 Comparison of present LSFs with linear slopes of Li et al. (2009) based on PS approach for $m_i = 15$, $D = 0$, and $k_v = 0$: **a** $k_h = 0.1$; **b** $k_h = 0.2$; **c** $k_h = 0.3$

$$\sigma_{ng} = q\left[\left(1 \pm k_v\right)\cos^2 \chi - k_h \sin \chi \cos \chi\right] \tag{29a}$$

$$\tau_g = -q\left[\left(1 \pm k_v\right)\sin \chi \cos \chi + k_h \cos^2 \chi\right]. \tag{29b}$$

It is worth observing from Eq. (29a, 29b) that Eq. (29a, 29b) turns into Eq. (19a, 19b) as χ approaches to 0, indicating a horizontal top surface (OG). Figure 15b depicts the variation of LSFs under static ($k_h = 0$) and seismic ($k_h = 0.2$) conditions for various values of χ. For both conditions, the LSFs are seen to acquire flat layouts as the magnitude of χ increases. It may be attributed to the fact that the inclined top surface exerts greater driving forces on the slope due to surplus rock mass. However, the impact of χ on the limiting stability is not found to be significant. Later, the stability of a rock-cut slope with an inclined top surface from the field is analyzed using the LSF concept to showcase the legitimacy of the proposed method.

5 Comparison

The current methodology demonstrates the slope stability analysis considering the concept of the LSF (FS = 1.0). Hence, a direct quantitative comparison with the available studies is difficult as the previous investigations focused on the minimum FS. However, considering different seismic approaches (PS, OPD, and MPD), the present results are compared qualitatively with the available studies (Li et al. 2009; Jiang et al. 2016; Qin and Chian 2018; Sarkar and Chakraborty 2021; Zhong and Yang 2021) in Figs. 16, 17, 18, 19, 20. Using the lower and the upper bound FELA coupled with the PS approach, Li et al. (2009) provided a set of stability charts based on the stability number, $N = \sigma_{ci}/(\gamma h.FS)$. Jiang et al. (2016) and Sarkar and Chakraborty (2021) recommended similar stability charts based on an explicit definition of the FS but under the framework
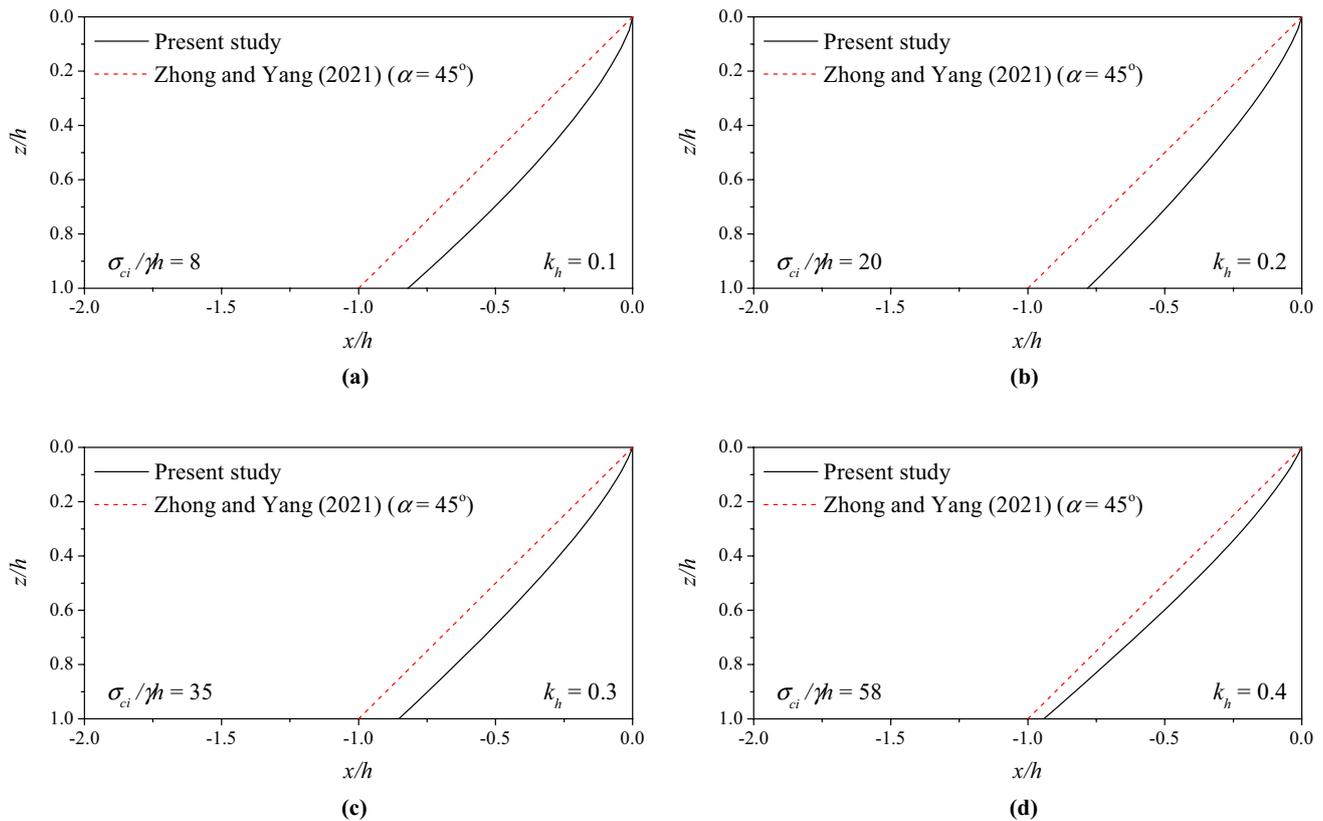
Fig. 17 Comparison of present LSFs with linear slopes of Zhong and Yang (2021) based on MPD approach for $GSI = 10$, $m_i = 15$, $D = 0$, $k_v = 0$, $\omega h/V_s = 0.63$, and $\xi = 0.15$: **a** $k_h = 0.1$; **b** $k_h = 0.2$; **c** $k_h = 0.3$; **d** $k_h = 0.4$

of the limit equilibrium (LE) and the variational limit equilibrium (VLE) methods, respectively. Qin and Chian (2018) employed a discretization-based kinematic approach of the limit analysis (LA) alongside the OPD approach to determine the seismic ultimate bearing capacity ($q/\gamma h$) of rock slopes. Further, Zhong and Yang (2021) implemented a combined framework of the kinematic approach of the LA and the MPD approach to revisit the seismic stability of rock slopes in terms of the critical stability number, $N_{cr} = \sigma_{ci}/\gamma h$, at FS = 1.0. Whatever the solution strategy, all the studies mentioned above considered a predetermined slope geometry, primarily linear, to commence with the analysis. In contrast, the present analysis surpasses such restriction by deriving the curvilinear LSF with the inputs taken from various available studies. Hence, considering different rock mass properties and seismic loading parameters, rational comparisons between the current LSFs and the linear slopes adopted by the available studies (Li et al. 2009; Jiang et al. 2016; Qin and Chian 2018; Sarkar and Chakraborty 2021; Zhong and Yang 2021) are presented in Figs. 16, 17, 18, 19, 20. It can be conceived from the comparison that the present curvilinear LSF mainly reveals a steeper gradient compared to the traditional linear slope considered by various

researchers, except for Qin and Chian (2018). In Figs. 16 and 17, the current LSFs obtained from the PS and the MPD approaches, respectively, compare reasonably well with the linear slopes ($\alpha = 45°$ and $60°$) adopted by Li et al. (2009) and Zhong and Yang (2021), where α is the horizontal inclination of the linear slope. Such a close agreement of the present LSFs with the linear slopes considered by previous researchers authenticates the accuracy and robustness of the proposed methodology. In Fig. 18, the current LSFs at higher values of GSI are found to be marginally flat compared to the linear slope assumed by Qin and Chain (2018) with $\alpha = 50°$. It may be attributed to the linearization of the GHB envelope through a generalized tangential technique by Qin and Chian (2018), which eventually overestimates the rock strength. Sarkar and Chakraborty (2021) followed a similar GHB envelope linearization process through the equivalent Mohr–Coulomb criterion. However, in the investigation of Sarkar and Chakraborty (2021), the effect of the rock strength overestimation successively subjugates through enhanced driving forces developed in an enlarged failure domain evolved with the VLE method. On the contrary, Jiang et al. (2016) considered predefined circular slip surfaces for the analysis based on the LE method. Hence, it can be seen from Fig. 19 that the current LSFs derived
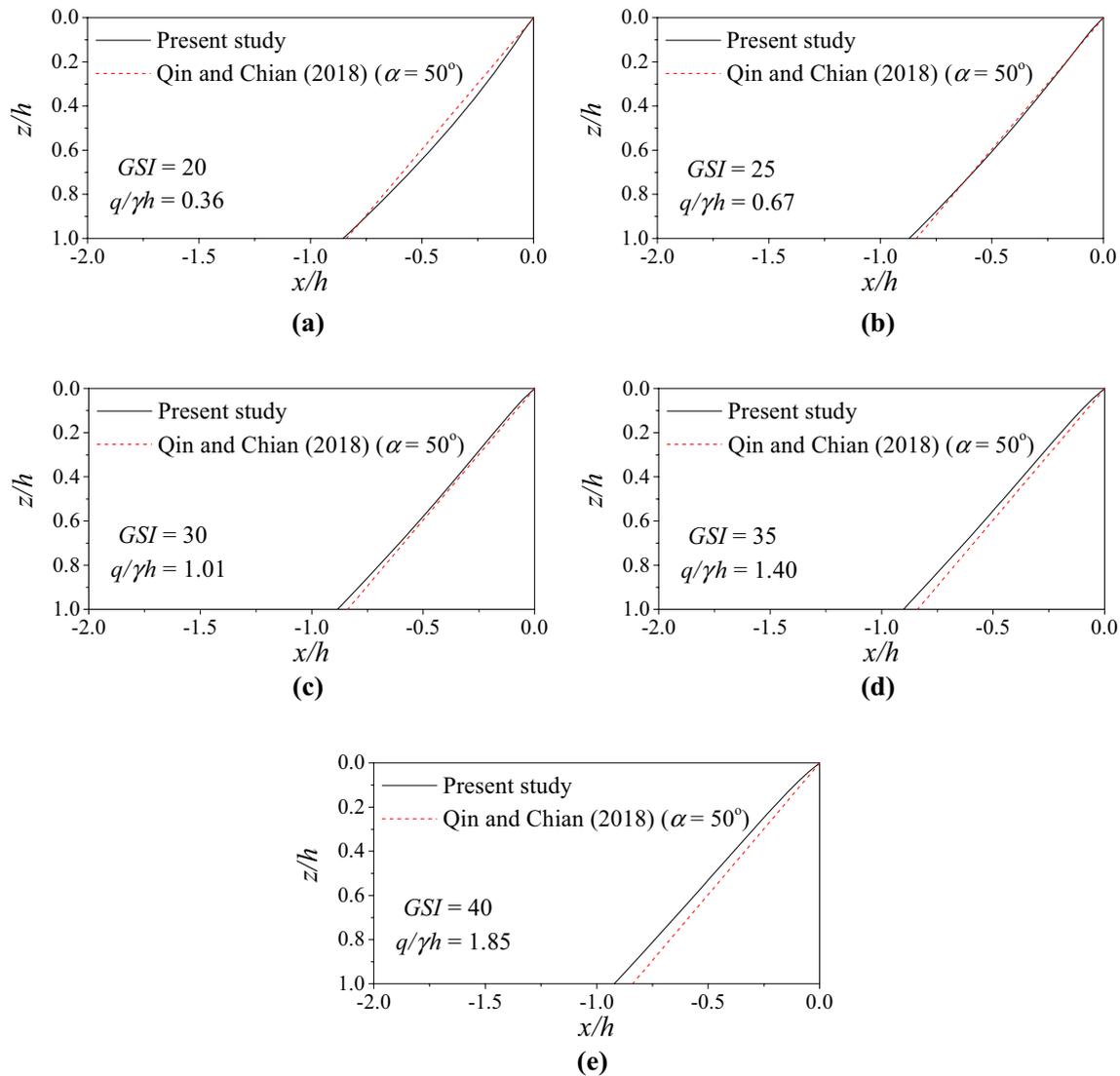
Fig. 18 Comparison of present LSFs with linear slopes of Qin and Chian (2018) based on OPD approach for $\sigma_c/\gamma h = 8$, $m_i = 10$, $D = 0$, $k_h = 0.1$, $k_v = 0.5k_h$, $\omega h/V_s = 0.79$, $\omega h/V_p = 0.46$, and $f_a = 1.0$: **a** $GSI = 20$; **b** $GSI = 25$; **c** $GSI = 30$; **d** $GSI = 35$; **e** $GSI = 40$

for the PS approach are steeper than the linear slopes ($\alpha = 30°$) considered by Jiang et al. (2016) and Sarkar and Chakraborty (2021).

In addition to the LSF, the critical slip surface (CSS) of rock slopes at the limiting equilibrium is also a primary concern of practicing engineers. Figure 20 compares the CSSs and LSFs obtained from this study with those reported by Qin and Chian (2018) at various seismicity levels. It can be seen from Fig. 20 that at lower seismicity levels, the current LSFs and CSSs differ significantly from those obtained by Qin and Chian (2018). However, a good agreement with Qin and Chian (2018) can be found as the seismicity level rises. Qin and Chian (2018) considered a strip footing resting with a set-back distance from the slope crest while determining the seismic ultimate bearing capacity ($q/\gamma h$) of linear rock slope ($\alpha = 50°$). In contrast, the

present work considers a comparable magnitude of surcharge ($q/\gamma h$) but starts from the slope crest (O) to derive the LSF. Apart from that, Qin and Chian (2018) adopted the generalized tangential technique to linearize the GHB criterion, which, as previously mentioned, further influences variation by overestimating the rock mass strength.

6 Application to Real Slopes

The proposed LSF concept is applied to analyze the seismic stability of various real slopes, as listed in Table 2. The analysis procedure primarily relies upon a profile-matching scheme, as illustrated by Nandi et al. (2021b). Accordingly, the LSF corresponding to the
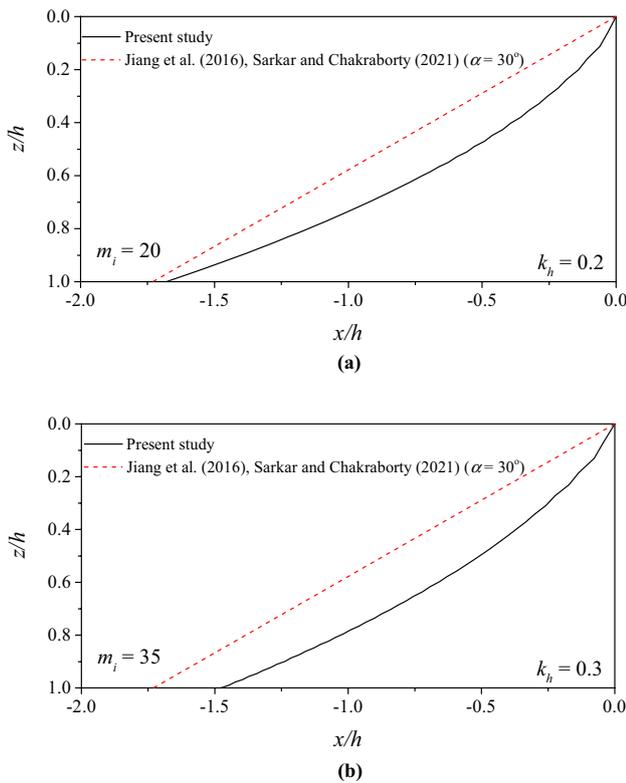
Fig. 19 Comparison of present LSFs with linear slopes of Jiang et al. (2016) and Sarkar and Chakraborty (2021) based on PS approach for $\sigma_{ci}/\gamma h = 1.0$, $GSI = 20$, $D = 0$, and $k_v = 0$: **a** $k_h = 0.2$; **b** $k_h = 0.3$

target FS of unity is first determined with the given rock mass properties and seismic inputs and then matched with the existing rock slope profile. Later, the stability of the slope can be assessed by examining the safety margin between the known profile and the derived profile. If the existing profile is found to be flat compared to the derived LSF (FS = 1.0), it remains safe and stable. Following this principle, the case study on the Donghekou landslide induced by the Wenchuan earthquake (2008) is revisited here. Among various landslides triggered by the Wenchuan earthquake, the Donghekou landslide located in Hongguang city of Qingchuan country was one of the large-scale rapid and long run-out landslides. The on-site acceleration records of the Wenchuan earthquake are shown in Fig. 21a. The geological conditions at the site are complex and mainly composed of metamorphic rocks and limestones (Zhao et al. 2017). The cross-section of the original slope in the Donghekou landslide is shown in Fig. 21b with the following details, $\alpha = 35°$ and $h = 360$ m (Zhang et al. 2015). As reported by Zhao et al. (2017), the geo-mechanical parameters of the rock mass at that site are mentioned in Table 2. However, more details of the location, such as groundwater table conditions and
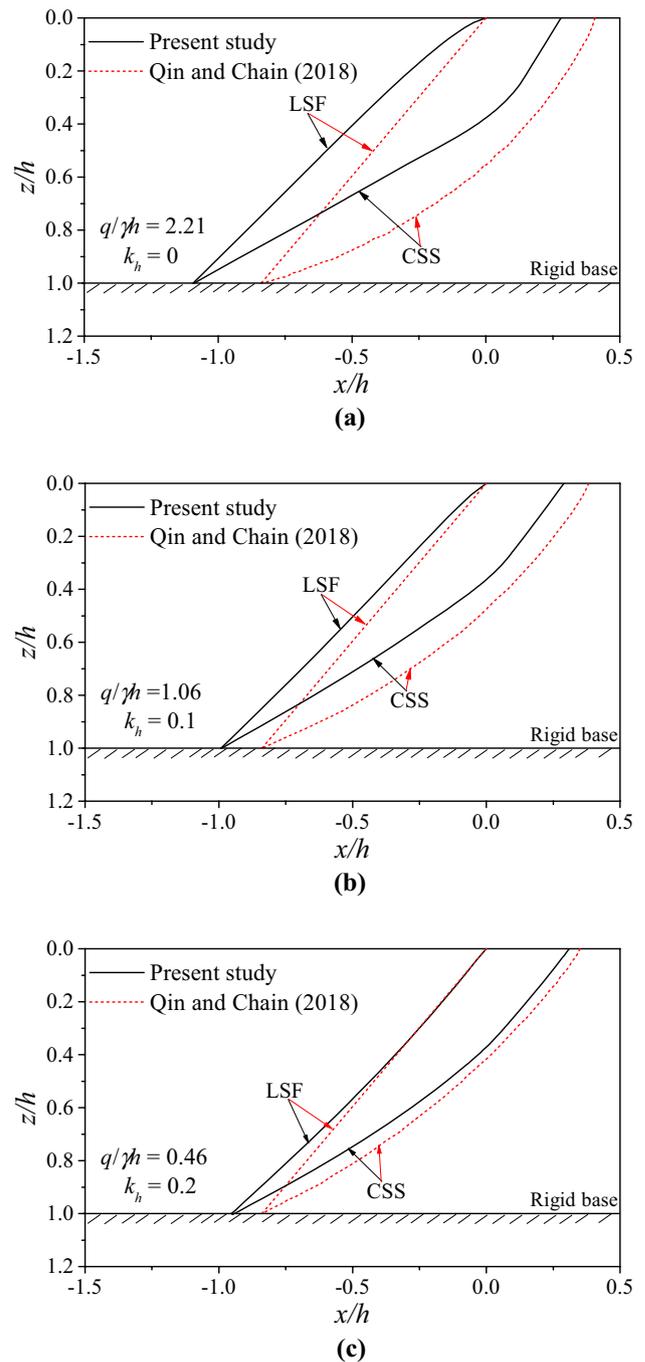

Fig. 20 Comparison of present LSFs and CSSs with Qin and Chian (2018) based on OPD approach for $\sigma_{ci}/\gamma h = 8$, $GSI = 30$, $m_i = 10$, $D = 0$, $k_v = 0.5k_h$, $\omega h/V_s = 0.79$, $\omega h/V_p = 0.46$, and $f_a = 1.5$: **a** $k_h = 0$; **b** $k_h = 0.1$; **c** $k_h = 0.2$

weathering parameters, can be obtained from earlier studies (Sun et al. 2012; Zhang et al. 2015; Zhao et al. 2017). Previous researchers (Sun et al. 2012; Zhang et al. 2015; Zhao et al. 2017) studied the Donghekou landslide using various techniques to consider wide-ranging and

deadliest causalities. Zhao et al. (2017) determined the slope displacement accumulated during the seismic event using the upper bound LA and the rigid block displacement technique. In the rigid block displacement technique, the displacement starts accumulating as the limiting stability of a given slope under the seismic condition exceeds. Accordingly, Zhao et al. (2017) reported no permanent displacement up to $t = 15$ s. The displacement accumulation began only at $t = 15$ s, followed by a devastating landslide. Hence, it can be reasonably assumed that the rock slope was marginally stable up to $t = 15$ s. At $t = 15$ s, seismic inertia forces induced by earthquake acceleration magnitudes of 0.22 g and -0.14 g in the horizontal and vertical directions, respectively, as indicated in Fig. 21a, surpassed the limiting stability (FS = 1.0) and pushed the slope toward imminent collapse. By employing these parameters as inputs (Table 2), the LSFs are derived based on the present analysis under static and pseudo-static conditions and compared with the original slope ($\alpha = 35°$) of the Donghekou landslide in Fig. 21c. Figure 21c indicates that the current LSF derived for the static condition is steeper than the original Donghekou slope. Hence, the Donghekou slope remained stable as long as there was no seismic evidence. However, in the presence of seismic excitation, the Donghekou slope urged for a flat profile to maintain the state of limiting stability (FS = 1.0), which can be seen from the present LSF under the pseudo-static condition. Since such a flat, curved slope profile was not satisfied with the comparatively steeper Donghekou linear slope with $\alpha = 35°$ (Fig. 21c), the slope led to an imminent collapse accompanied by a large co-seismic displacement as previously investigated by Zhao et al. (2017).

The seismic stability of the right abutment slope of the Chenab railway bridge in the Himalayas, India (Latha and Garaga 2010) and a cut slope along the National Highway (NH – 7) in Uttarakhand, India (Singh et al. 2022) is examined using the present LSF concept. The input parameters required for this analysis are adopted from relevant literature and mentioned in Table 2. It is worth noting that some surcharge loads from the bridge piers were considered while analyzing the stability of the right abutment of the Chenab railway bridge (Latha and Garaga 2010). However, in this study, such surcharge loads are neglected due to their nominal values. In Fig. 22, the LSFs obtained from the current analyses are noticed to compare reasonably well with the existing profiles for both cases. Consequently, these slopes are marginally stable based on FS of 1.0. Latha and Garaga (2010) and Singh et al. (2022) also reported similar results with FS values of 1.02 and 0.995, respectively. Thus, the current LSF-based stability criterion establishes an efficient and expedient benchmark for the stability analysis of existing rock slopes.

Table 2 Input parameters used for validating various case studies

Case studies	References	Input parameters										
		σ_{ci} (MPa)	GSI	m_i	D	γ (kN/m³)	h (m)	$\sigma_{ci}/\gamma h$	m_b	s	k_h	k_v
Donghekou landslide, Hongguang, Qingchuan	Zhao et al. (2017)	45	45	8	1.0	23	360	5.4	0.157	1.04E-04	0.22	– 0.14
Right abutment of Chenab railway bridge, Himalayas, India	Latha and Garaga (2010)	115	43	23.52	–	27	350	12.2	0.59	1.27E-03	0.31	– 0.20
Cut slope, National Highway (NH)-7, Uttarakhand, India	Singh et al. (2022)	62.8	41	10	1.0	27	40[a]	58.1	0.148	5.36E-05	0.26	0.15

[a]Top surface of the slope is inclined to the horizontal at an angle (χ) of approximately 11°, and hence, the slope height (h) is measured from the toe (A) to the crest (O) of the slope
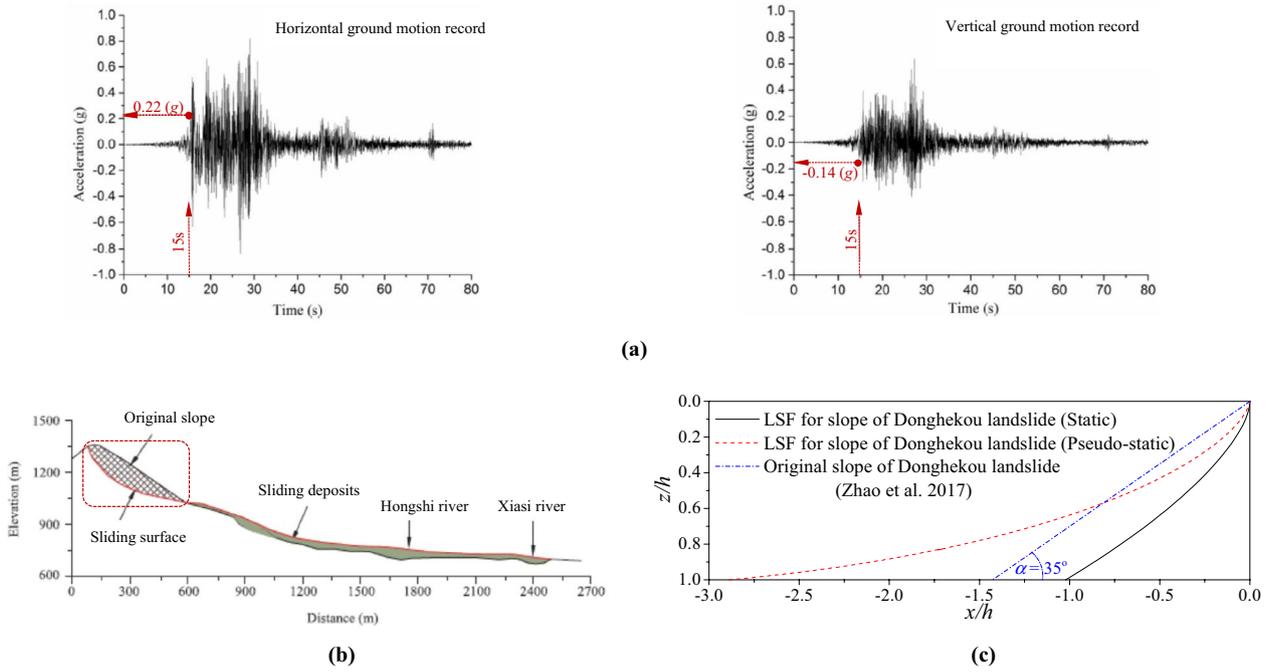
Fig. 21 **a** Accelerations of Whenchuan earthquake (Zhao et al. 2017); **b** cross-section of the Donghekou landslide (Zhang et al. 2015); **c** comparison of present LSFs with the original slope in Donghekou landslide (Zhao et al. 2017) based on PS approach
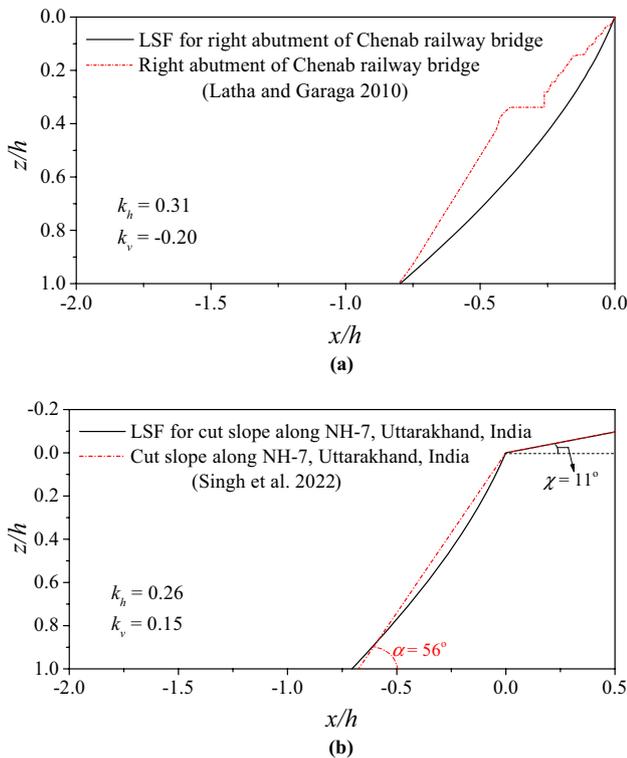

Fig. 22 Comparison of present LSFs under PS condition with **a** the slope of right abutment of Chenab railway bridge, Himalayas, India (Latha and Garaga 2010); **b** the rock-cut slope along NH-7, Uttarakhand, India (Singh et al. 2022)

7 Conclusions

An integrated framework of the method of stress characteristics (MSC), the modified pseudo-dynamic (MPD) approach, and the generalized Hoek–Brown (GHB) strength criterion is effectively implemented in this paper to predict the limiting seismic stability of rock slopes. Traditional stability indices, such as stability number and factor of safety, are replaced with the concept of the limiting slope face (LSF). The current methodology obliterates the demand for prejudged geometry of the slope face and the slip surface. Compared to the traditional linear slopes, the derived LSFs are found to provide an optimized solution with a factor of safety of 1.0. An extensive parametric study demonstrating the effect of various rock mass properties, seismic wave parameters, rigid variable base, and inclined top surface imparts a better insight into the limiting behavior of rock slopes. The LSF-based design charts are provided to assess the seismic stability of rock slopes efficiently. For the advancements in rock slope engineering, the LSF concept is applied to different case studies, advocating the practical implications of the proposed technique. The present study focuses on determining slope faces at the limiting stability (FS = 1.0), whereas in standard design practice, slope faces with FS > 1.0 are generally reported. Hence, this study can be extended further by coupling it with an appropriate strength reduction strategy to obtain higher FS.

Declarations

Conflict of Interest The authors have no relevant financial or non-financial interests to disclose. The authors have no competing interests to declare that are relevant to the content of this article. All authors certify that they have no affiliations with or involvement in any organization or entity with any financial interest or non-financial interest in the subject matter or materials discussed in this manuscript. The authors have no financial or proprietary interests in any material discussed in this article.

References

Belghali M, Saada Z, Garnier D, Maghous S (2017) Pseudo-static stability analysis of rock slopes reinforced by passive bolts using the generalized Hoek-Brown criterion. J Rock Mech Geotech Eng 9(4):659–670. https://doi.org/10.1016/j.jrmge.2016.12.007

Bellezza I (2014) A new pseudo-dynamic approach for seismic active soil thrust. Geotech Geol Eng 32(2):561–576. https://doi.org/10.1007/s10706-014-9734-y

Bellezza I (2015) Seismic active earth pressure on walls using a new pseudo-dynamic approach. Geotech Geol Eng 33(4):795–812. https://doi.org/10.1007/s10706-015-9860-1

Booker JR, Davis EH (1972) A general treatment of plastic anisotropy under conditions of plane strain. J Mech Phys Solids 20(4):239–250

Choudhury D, Nimbalkar S (2005) Seismic passive resistance by pseudo-dynamic method. Géotechnique 55(9):699–702. https://doi.org/10.1680/geot.2005.55.9.699

Fan G, Zhang L, Zhang J, Yang C (2019) Analysis of seismic stability of an obsequent rock slope using time–frequency method. Rock Mech Rock Eng 52:3809–3823. https://doi.org/10.1007/s00603-019-01821-9

Fu W, Liao Y (2010) Non-linear shear strength reduction technique in slope stability calculation. Comput Geotech 37(3):288–298. https://doi.org/10.1016/j.compgeo.2009.11.002

Gischig VS, Eberhardt E, Moore JR, Hungr O (2015) On the seismic response of deep-seated rock slope instabilities – insights from numerical modeling. Eng Geol 193:1–18. https://doi.org/10.1016/j.enggeo.2015.04.003

Gray DH (2013) Influence of slope morphology on the stability of earthen slopes. In: Proceedings of Geo-Congress 2013, Reston, VA, pp 1902–1911

Gu XB, Wu QH (2019) Seismic stability analysis of waterfront rock slopes using the modified pseudo-dynamic method. Geotech Geol Eng 37(3):1743–1753. https://doi.org/10.1007/s10706-018-0718-1

Hoek E, Brown ET (1980) Empirical strength criterion for rock masses. J Geotech Eng Div ASCE 106(9):1013–1035. https://doi.org/10.1061/AJGEB6.0001029

Hoek E, Brown ET (1997) Practical estimates of rock mass strength. Int J Rock Mech Min Sci 34(8):1165–1186. https://doi.org/10.1016/S1365-1609(97)80069-X

Hoek E, Carranza-Torres C, Corkum B (2002) Hoek-brown failure criterion – 2002 edition. In: Proceedings of the 5th North American rock mechanics symposium, Toronto, pp 267–273

Jahanandish M, Keshavarz A (2005) Seismic bearing capacity of foundations on reinforced soil slopes. Geotext Geomembr 23(1):1–25. https://doi.org/10.1016/j.geotexmem.2004.09.001

Jiang XY, Cui P, Liu CZ (2016) A chart-based seismic stability analysis method for rock slopes using Hoek-Brown failure criterion. Eng Geol 209:196–208. https://doi.org/10.1016/j.enggeo.2016.05.015

Keshavarz A, Kumar J (2018) Bearing capacity of foundations on rock mass using the method of characteristics. Int J Numer Anal Methods Geomech 42(3):542–557. https://doi.org/10.1002/nag.2754

Keshavarz A, Kumar J (2021) Bearing Capacity of ring foundations over rock media. J Geotech Geoenviron Eng 147(6):04021027. https://doi.org/10.1061/(ASCE)GT.1943-5606.0002517

Keshavarz A, Fazeli A, Sadeghi S (2016) Seismic bearing capacity of strip footings on rock masses using the Hoek-Brown failure criterion. J Rock Mech Geotech Eng 8(2):170–177. https://doi.org/10.1016/j.jrmge.2015.10.003

Kramer SL (1996) Geotechnical earthquake engineering. Prentice Hall, Upper Saddle River, New Jersey

Kumar J, Chakraborty D (2013) Seismic bearing capacity of foundations on cohesionless slopes. J Geotech Geoenviron Eng 139(11):1986–1993. https://doi.org/10.1061/(ASCE)GT.1943-5606.0000909

Kumar J, Mohan Rao VBK (2003) Seismic bearing capacity of foundations on slopes. Géotechnique 53(3):347–361. https://doi.org/10.1680/geot.2003.53.3.347

Kumar J, Rahaman O (2020) Lower bound limit analysis using power cone programming for solving stability problems in rock mechanics for generalized Hoek-Brown criterion. Rock Mech Rock Eng 53:3237–3252. https://doi.org/10.1007/s00603-020-02099-y

Latha GM, Garaga A (2010) Seismic stability analysis of a Himalayan rock slope. Rock Mech Rock Eng 43:831–843. https://doi.org/10.1007/s00603-010-0088-3

Li AJ, Lyamin AV, Merifield RS (2009) Seismic rock slope stability charts based on limit analysis methods. Comput Geotech 36(1–2):135–148. https://doi.org/10.1016/j.compgeo.2008.01.004

Li C, Jiang P, Zhou A (2019) Rigorous solution of slope stability under seismic action. Comput Geotech 109:99–107. https://doi.org/10.1016/j.compgeo.2019.01.018

Li C, Wei S, Xu X, Qu X (2022) Modelling of critical acceleration for regional seismic landslide hazard assessments by finite element limit analysis. Front Earth Sci. https://doi.org/10.3389/feart.2022.830371

Luo Y, Fan X, Huang R, Wang Y, Yunus AP, Havenith HB (2020) Topographic and near-surface stratigraphic amplification of the seismic response of a mountain slope revealed by field monitoring and numerical simulations. Eng Geol 271:105607. https://doi.org/10.1016/j.enggeo.2020.105607

Mononobe N, Matsuo H (1929) On the determination of earth pressure during earthquake. In: Proceedings of World Engineering Conf, Tokyo, Japan, pp 177–185

Nandi S, Santhoshkumar G, Ghosh P (2021a) Determination of critical slope face in c–ϕ soil under seismic condition using

method of stress characteristics. Int J Geomech 21(4):04021031. https://doi.org/10.1061/(ASCE)GM.1943-5622.0001976

Nandi S, Santhoshkumar G, Ghosh P (2021b) Development of limiting soil slope profile under seismic condition using slip line theory. Acta Geotech 16(11):3517–3531. https://doi.org/10.1007/s11440-021-01251-4

Nimbalkar SS, Choudhury D, Mandal JN (2006) Seismic stability of reinforced-soil wall by pseudo-dynamic method. Geosynth Int 13(3):111–119. https://doi.org/10.1680/gein.2006.13.3.111

Okabe S (1926) General theory of earth pressure. J Jpn Soc Civ Eng 12(6):1277–1323

Pain A, Choudhury D, Bhattacharyya SK (2017) Seismic rotational stability of gravity retaining walls by modified pseudo-dynamic method. Soil Dyn Earthq Eng 94:244–253. https://doi.org/10.1016/j.soildyn.2017.01.016

Qin C, Chian SC (2018) Seismic ultimate bearing capacity of a Hoek-Brown rock slope using discretization-based kinematic analysis and pseudodynamic methods. Int J Geomech 18(6):04018054. https://doi.org/10.1061/(asce)gm.1943-5622.0001147

Rajesh BG, Choudhury D (2017) Seismic passive earth resistance in submerged soils using modified pseudo-dynamic method with curved rupture surface. Mar Georesources Geotechnol 35(7):930–938. https://doi.org/10.1080/1064119X.2016.1260077

Renani HR, Martin CD (2020) Slope stability analysis using equivalent Mohr-Coulomb and Hoek-Brown criteria. Rock Mech Rock Eng 53:13–21. https://doi.org/10.1007/s00603-019-01889-3

Santhoshkumar G, Ghosh P (2020) Seismic stability analysis of a hunchbacked retaining wall under passive state using method of stress characteristics. Acta Geotech 15(10):2969–2982. https://doi.org/10.1007/s11440-020-01003-w

Santhoshkumar G, Ghosh P, Murakami A (2019) Seismic active resistance of a tilted cantilever retaining wall considering adaptive failure mechanism. Int J Geomech 19(8):04019086. https://doi.org/10.1061/(ASCE)GM.1943-5622.0001470

Sarkar S, Chakraborty M (2021) Pseudostatic stability analysis of rock slopes using variational method. Indian Geotech J 51(5):935–951. https://doi.org/10.1007/s40098-020-00475-7

Serrano A, Olalla C (1994) Ultimate bearing capacity of rock masses. Int J Rock Mech Min Sci Geomech Abstr 31(2):93–106. https://doi.org/10.1016/0148-9062(94)92799-5

Serrano A, Olalla C, González J (2000) Ultimate bearing capacity of rock masses based on the modified Hoek-Brown criterion. Int J Rock Mech Min Sci 37(6):1013–1018. https://doi.org/10.1016/S1365-1609(00)00028-9

Shen J, Priest SD, Karakus M (2012) Determination of Mohr-Coulomb shear strength parameters from generalized Hoek-Brown criterion for slope stability analysis. Rock Mech Rock Eng 45(1):123–129. https://doi.org/10.1007/s00603-011-0184-z

Singh HM, Singh TN, Singh KH (2022) Integrated empirical and numerical approach for stability and failure analysis of cut slopes in seismically active Uttarakhand Himalayan, India. Eng Fail Anal 131:105847. https://doi.org/10.1016/j.engfailanal.2021.105847

Sokolovski VV (1960) Statics of soil media. Butterworths Scientific Publications, London

Srikar G, Mittal S (2020) Seismic analysis of retaining wall subjected to surcharge: a modified pseudodynamic approach. Int J Geomech 20(9):06020022. https://doi.org/10.1061/(ASCE)GM.1943-5622.0001780

Steedman RS, Zeng X (1990) The influence of phase on the calculation of pseudo-static earth pressure on a retaining wall. Géotechnique 40(1):103–112. https://doi.org/10.1680/geot.1990.40.1.103

Sun P, Yin Y, Wu S, Chen L (2012) Does vertical seismic force play an important role for the failure mechanism of rock avalanches? A case study of rock avalanches triggered by the Wenchuan earthquake of May 12, 2008, Sichuan China. Environ Earth Sci 66(5):1285–1293. https://doi.org/10.1007/s12665-011-1338-8

Sun C, Chai J, Luo T, Xu Z, Qin Y, Yuan X, Ma B (2020) Stability charts for pseudostatic stability analysis of rock slopes using the non-linear Hoek-Brown strength reduction technique. Adv Civil Eng. https://doi.org/10.1155/2020/8841090

Sun ZB, Wang BW, Hou CQ, Wu SC, Yang XL (2022) Pseudodynamic approach for rock slopes in Hoek-Brown media: three-dimensional perspective. Int J Geomech 22(11):04022190. https://doi.org/10.1061/(ASCE)GM.1943-5622.0002553

Tiwari G, Latha GM (2016) Design of rock slope reinforcement: an Himalayan case study. Rock Mech Rock Eng 49:2075–2097. https://doi.org/10.1007/s00603-016-0913-4

Veiskarami M, Kumar J, Valikhah F (2014) Effect of the flow rule on the bearing capacity of strip foundations on sand by the upper-bound limit analysis and slip lines. Int J Geomech 14(3):04014008. https://doi.org/10.1061/(ASCE)GM.1943-5622.0000324

Wallace CS, Schaefer LN, Villeneuve MC (2022) Material properties and triggering mechanisms of an andesitic lava dome collapse at Shiveluch Volcano, Kamchatka, Russia, revealed using the finite element method. Rock Mech Rock Eng 55:2711–2728. https://doi.org/10.1007/s00603-021-02513-z

Wang B, Li T, Sun Z, Li Y, Hou C (2022a) A pseudo-dynamic approach for seismic stability analysis of rock slopes in Hoek-Brown media. Geotech Geol Eng 40(7):3561–3577. https://doi.org/10.1007/s10706-022-02120-x

Wang S, Zhang Z, Huang X, Lei Q (2022b) Generalized block theory for the stability analysis of blocky rock mass systems under seismic loads. Rock Mech Rock Eng 55:2747–2769. https://doi.org/10.1007/s00603-021-02628-3

Wu G, Zhao M, Zhang R, Lei M (2021) Ultimate bearing capacity of strip footings on Hoek-Brown rock slopes using adaptive finite element limit analysis. Rock Mech Rock Eng 54:1621–1628. https://doi.org/10.1007/s00603-020-02334-6

Wu W, Utili S (2015) On the optimal profile of a rock slope. In: Proceedings of the 13th international congress of rock mechanics, Montreal, Canada

Xu X, Zhou X, Huang X, Xu L (2017) Wedge-failure analysis of the seismic slope using the pseudodynamic method. Int J Geomech 17(12):04017108. https://doi.org/10.1061/(ASCE)GM.1943-5622.0001015

Xu J, Pan Q, Yang XL, Li W (2018) Stability charts for rock slopes subjected to water drawdown based on the modified non-linear Hoek-Brown failure criterion. Int J Geomech 18(1):04017133. https://doi.org/10.1061/(ASCE)GM.1943-5622.0001039

Yang XL, Zou JF (2006) Stability factors for rock slopes subjected to pore water pressure based on the Hoek-Brown failure criterion. Int J Rock Mech Min Sci 43(7):1146–1152. https://doi.org/10.1016/j.ijrmms.2006.03.010

Yang XL, Li L, Yin JH (2004) Seismic and static stability analysis for rock slopes by a kinematical approach. Géotechnique 54(8):543–549. https://doi.org/10.1680/geot.2004.54.8.543

Zeng X, Steedman RS (1993) On the behaviour of quay walls in earthquakes. Géotechnique 43(3):417–431. https://doi.org/10.1680/geot.1993.43.3.417

Zhang Y, Wang J, Xu Q, Chen G, Zhao JX, Zheng L, Han Z, Yu P (2015) DDA validation of the mobility of earthquake-induced landslides. Eng Geol 194:38–51. https://doi.org/10.1016/j.enggeo.2014.08.024

Zhao L, Cheng X, Li L, Chen J, Zhang Y (2017) Seismic displacement along a log-spiral failure surface with crack using rock Hoek-Brown failure criterion. Soil Dyn Earthq Eng 99:74–85. https://doi.org/10.1016/j.soildyn.2017.04.019

Zhao L, Yu C, Li L, An A, Nie Z, Peng A, Zuo S (2020) Rock slope reliability analysis using Barton-Bandis failure criterion with

modified pseudo-dynamic approach. Soil Dyn Earthq Eng 139:106310. https://doi.org/10.1016/j.soildyn.2020.106310

Zhong JH, Yang XL (2021) Pseudo-dynamic stability of rock slope considering Hoek-Brown strength criterion. Acta Geotech 17(6):2481–2494. https://doi.org/10.1007/s11440-021-01425-0